Atmos. Chem. Phys. Discuss., doi:10.5194/acp-2016-247, 2016
Manuscript under review for journal Atmos. Chem. Phys.
Published: 5 April 2016

Atmospheric Chemistry and Physics Discussions

Heterogeneous Kinetics of H_2O, HNO_3 and HCl on HNO_3 hydrates (α-NAT, β-NAT, NAD) in the range 175-200 K

Riccardo Iannarelli[1,2] and Michel J. Rossi[1]

[1]Laboratory of Atmospheric Chemistry (LAC), Paul Scherrer Institute (PSI), CH-5232 PSI Villigen, Switzerland; [2]New address: Safety, Prevention and Health Domain, RI DSPS-SCC , Station 6, Ecole Polytechnique Fédérale de Lausanne (EPFL), CH-1015 Ecublens, Switzerland.

Correspondence to: M. J. Rossi (michel.rossi@psi.ch)

Abstract

Experiments on the title compounds have been performed using a multidiagnostic stirred-flow reactor (SFR) in which the gas- as well as the condensed phase has been simultaneously investigated under stratospheric temperature conditions in the range 175-200 K. Wall interactions of the title compounds have been taken into account using Langmuir adsorption isotherms in order to close the mass balance between deposited and desorbed (recovered) compounds. Thin solid films at 1 μm typical thickness have been used as a proxy for atmospheric ice particles and have been deposited on a Si window of the cryostat where the optical element was the only cold point in the deposition system. FTIR absorption spectrometry in transmission as well as partial and total pressure measurement using residual gas MS and sensitive pressure gauges have been employed in order to monitor growth and evaporation processes as a function of temperature using both pulsed gas admission and continuous monitoring under SFR conditions. Thin solid H_2O ice films were used as the starting point throughout, with the initial formation of α-NAT followed by the gradual transformation of α- ➔ β-NAT starting at 185 K. NAD was formed at once at somewhat larger partial pressures of HNO_3 deposited on pure H_2O ice. In contrast to published reports the formation of α-NAT proceeded without prior formation of an amorphous HNO_3/H_2O layer and always resulted in β-NAT. For α- and β-NAT the temperature dependent accommodation coefficient $\alpha(H_2O)$ and $\alpha(HNO_3)$, the evaporation flux $J_{ev}(H_2O)$ and $J_{ev}(HNO_3)$ and the resulting saturation vapor pressure $P_{eq}(H_2O)$ and $P_{eq}(HNO_3)$ were measured and compared to binary phase diagrams of HNO_3/H_2O in order to afford

Atmos. Chem. Phys. Discuss., doi:10.5194/acp-2016-247, 2016
Manuscript under review for journal Atmos. Chem. Phys.
Published: 5 April 2016

Atmospheric Chemistry and Physics Discussions

thermochemical control of the kinetic parameters. The resulting kinetic and thermodynamic parameters of activation energies for evaporation (E_{ev}) and standard heats of evaporation ΔH_{ev}^{0} of H_2O and HNO_3 for α- and β-NAT, respectively, led to an estimate for the relative standard enthalpy difference between α- and β-NAT of -6.0 ± 20 kJ/mol in favor of β-NAT, as expected, despite a significantly larger value of E_{ev} for HNO_3 in α-NAT. This in turn implies a substantial activation energy for HNO_3 accommodation in α- compared to β-NAT where $E_{acc}(HNO_3)$ is essentially zero. The kinetic ($\alpha(HCl)$, $J_{ev}(HCl)$) and thermodynamic ($P_{eq}(HCl)$) parameters of HCl-doped α- and β-NAT have been determined under the assumption that HCl adsorption did not significantly affect $\alpha(H_2O)$ and $\alpha(HNO_3)$ as well as the evaporation flux $J_{ev}(H_2O)$. $J_{ev}(HCl)$ and $P_{eq}(HCl)$ on both α- and β-NAT are larger than the corresponding values for HNO_3 across the investigated temperature range but significantly smaller than the values for pure H_2O ice. This means that once contaminated with HCl the "impurity" HCl will persist along with HNO_3 upon complete evaporation of the atmospheric ice particle. We comment on recent laboratory results involving the HNO_3/H_2O system using Chilled Mirror Hygrometers (CMH) in light of the present kinetic results.

1 Introduction

Heterogeneous processes taking place on ice clouds in the Upper Troposphere (UT) or on Polar Stratospheric Clouds (PSC's) in the Lower Stratosphere (LS) have, since a long time, been recognized as one of the major ozone depleting mechanism (Solomon et al., 1986). PSC's consist of either particles of crystalline nitric acid trihydrate (NAT) (type Ia), ternary $H_2SO_4/HNO_3/H_2O$ supercooled solutions (type Ib) or pure H_2O ice (type II) (Zondlo et al. 2000) and are formed during the polar winter season when temperatures are sufficiently low in order to allow H_2O supersaturation that ultimately leads to cloud formation in the dry stratosphere subsequent to ice nucleation (Peter, 1997).

Ozone is depleted during the Arctic and Antarctic spring season after unreactive chlorine reservoir compounds, $ClONO_2$ and HCl, are converted into molecular chlorine and rapidly photolyze into active atomic chlorine during the spring season (Solomon, 1990). The presence of PSC's enables heterogeneous chemical reactions such as Reaction (R1), which represents one of the most efficient stratospheric heterogeneous reactions (Friedl et al, 1986; Molina et al., 1985, 1987):

Atmos. Chem. Phys. Discuss., doi:10.5194/acp-2016-247, 2016
Manuscript under review for journal Atmos. Chem. Phys.
Published: 5 April 2016

Atmospheric Chemistry and Physics Discussions

$$ClONO_2(g) + HCl(s) \rightarrow Cl_2(g) + HNO_3(s) \quad (R1)$$

Reaction (R1) is orders of magnitude faster than the corresponding homogeneous gas phase process (Molina et al., 1985) and the most important chlorine-activating reaction in the polar stratosphere. The contribution to ozone destruction from Reaction (R1) is twofold: first, the released molecular Cl_2 rapidly photolyzes into atomic Cl establishing a cycle of O_3 destruction and, second, the overall removal of nitrogen oxides from the gas phase by entrapment of HNO_3 in the ice, facilitates O_3 destruction through a gas phase catalytic cycle similar to the one reported in Reactions (R2)-(R4):

$$X + O_3 \rightarrow XO + O_2 \quad (R2)$$

$$\underline{XO + O \rightarrow X + O_2} \quad (R3)$$

$$\text{net: } O_3 + O \rightarrow O_2 + O_2 \quad (R4)$$

where X is H, OH, NO, Cl or Br leading to HO_x, NO_x, ClO_x and BrO_x catalytic cycles, respectively.

Reaction (R1) increases the concentration of HNO_3 in the condensed phase and when PSC particles become sufficiently large and fall out of the stratosphere, active nitrogen is permanently removed through denitrification which has been observed in the field (Fahey et al., 2001). Lower concentrations of nitrate owing to the absence of HNO_3 inhibit reactions such as Reaction (R5):

$$ClO + NO_2 + M \rightarrow ClONO_2 + M \quad (R5)$$

which form reservoir species with longer atmospheric residence times.

The study of HNO_3 interaction with ice in the temperature and pressure ranges typical of the UT/LS is crucial in order to understand the de-nitrification process initiated by reaction (R1) and its effectiveness in the overall ozone destruction mechanism. To this purpose, many research groups (Voigt et al., 2000, 2005; Fahey et al., 2001; Schreiner et al., 2003; Gao et al., 2004; Höpfner et al., 2006) have studied the composition of PSC's using both *in situ* and remote sensing techniques both in the Arctic as well as above Antarctica. A balloonborne experiment at first detected non-crystalline HNO_3 hydrates (Schreiner et al., 1999), later both ballonborne (Voigt et al., 2000; Schreiner et al., 2003) and aircraft campaigns (Voigt et al., 2005) obtained unambiguous proof of the presence of crystalline HNO_3 hydrates (NAT) at altitudes between 18 and 24 km in the Arctic. The presence of β-NAT, through the

Atmos. Chem. Phys. Discuss., doi:10.5194/acp-2016-247, 2016
Manuscript under review for journal Atmos. Chem. Phys.
Published: 5 April 2016

identification of type Ia PSC's, has been unambiguously confirmed by Höpfner et al. (2006) using the MIPAS instrument on a satellite platform by comparison of measured limb-emission spectra of polar stratospheric clouds with measured optical constants in the region of the symmetric NO_3 peak at ν_2 = 820 cm^{-1}.

The existence of several crystalline hydrates of nitric acid has been confirmed for several years. Hanson and Mauersberger (1988) have identified two stable hydrates, namely, nitric acid monohydrate (NAM, $HNO_3 \bullet H_2O$) and nitric acid trihydrate (NAT, $HNO_3 \bullet 3H_2O$) by measuring the vapour pressure of mixtures of ice and HNO_3. The observed vapour pressures of HNO_3 and H_2O in the polar atmosphere indicate that only NAT may be of atmospheric importance. Several distinct crystalline hydrates of HNO_3 have been found by Ritzhaupt and Devlin (1991) in their work examining the infrared absorption spectrum of thin film samples. By depositing the equilibrium vapours of aqueous HNO_3 solutions of different concentrations at 293 K they observed nitric acid dihydrate (NAD, $HNO_3 \bullet 2H_2O$), NAM and NAT. Ji and Petit have performed an in-depth and ground-breaking investigation on the thermochemical properties of NAD (Ji and Petit, 1993).

Tolbert and coworkers have also reported infrared absorption spectra of NAM, NAD and NAT in a series of studies. Tolbert and Middlebrook (1990) have co-condensed calibrated mixtures of H_2O/HNO_3 vapours onto a cold support and assigned the absorption spectra of the growing thin films to nitric acid hydrates (NAM, NAD or NAT) according to the ratio of the dosing gases. Koehler et al. (1992) have observed the Fourier transform infrared (FTIR) absorption spectra in transmission of nitric acid hydrate thin films and measured their composition using temperature-programmed desorption (TPD). They confirmed the previously assigned spectra of NAD and NAM. They were also the first to observe two distinct structures of NAT: a low-temperature and metastable structure they called α-NAT and a thermodynamically stable high-temperature structure named β-NAT. Middlebrook et al. (1992) observed that NAD consistently converts to β-NAT when exposed to H_2O partial pressures typical of the stratosphere and therefore proposed that NAD is also metastable under stratospheric conditions.

Several other groups have investigated the structure of nitric acid hydrates and published absorption spectra of both α-NAT and β-NAT in the mid-IR range, using grazing incidence Reflection Absorption IR spectroscopy (RAIRS) (Zondlo et al., 1998; Zondlo et al., 2000;

Atmos. Chem. Phys. Discuss., doi:10.5194/acp-2016-247, 2016
Manuscript under review for journal Atmos. Chem. Phys.
Published: 5 April 2016

Ortega et al., 2003; Ortega et al., 2006; Herrero et al., 2006; Escribano et al., 2007) and FTIR in transmission (Tso and Leu, 1996; Martin-Llorente et al., 2006; Ortega et al., 2006).

The study of the phase diagram of the system H_2O/HNO_3 showed evidence that NAD may as well occur in at least two different structures (Beyer and Hansen, 2002). The two structures are both metastable and convert into NAM and NAT depending on experimental conditions. Grothe et al. (2004) also reported polymorphism of NAD where the formation of α-NAD or β-NAD strongly depended on the temperature of crystallization.

Compared to the molecular properties of the nitric acid hydrates knowledge of the kinetic parameters of trace gases interacting with HNO_3 hydrates is scarce. Middlebrook et al. (1992) have used time-dependent FTIR monitoring of the optical density of growing NAT films during deposition to measure the uptake of H_2O and HNO_3 on NAT. They reported a value of $\gamma_{NAT}(HNO_3) > 0.4$ for HNO_3 net uptake (γ) on NAT at T = 197 K whereas the range $2.0\times10^{-3} \leq \gamma_{NAT}(H_2O) \leq 1.0\times10^{-2}$ is reported for H_2O, respectively. The range measured for $\gamma_{NAT}(H_2O)$ corresponds to the HNO_3 pressure used during the deposition. Using evaporation experiments in a slow-flow reactor Biermann et al. (1998) measured the accommodation coefficient of H_2O on β-NAT substrates, $\alpha_{\beta-NAT}(H_2O)$, from the thickness of the substrate measured using FTIR absorption. They found no temperature dependence, reporting lower limiting values of $\alpha_{\beta-NAT}(H_2O) = (2.2 – 6.0)\times10^{-2}$ in the temperature range 192-202 K.

Delval and Rossi (2005) have used a multidiagnostic flow reactor, similar to the one used in this work, coupled with a quartz crystal microbalance (QCMB) for the measurement of the evaporation rate of H_2O from α-NAT and β-NAT thin films. They reported a positive temperature dependence of $\alpha_{\alpha-NAT}(H_2O)$ and a negative temperature dependence of $\alpha_{\beta-NAT}(H_2O)$ in the temperature range 179-208 K.

Hanson (1992) also measured the uptake coefficient of HNO_3 on NAT using a cold coated-wall flow tube with HNO_3 deposited on ice condensed on the cold flow tube walls and reported $\gamma_{NAT}(HNO_3) > 0.3$. A rapid uptake was observed which decreased as the surface coverage or dose of HNO_3 increased. Furthermore, the observed steady state partial pressure of HNO_3 over the ice substrate is about a factor of 5 higher than the HNO_3 vapor pressure over NAT and thus indicates that no hydrate was actually formed during the experiments. Therefore, the observed uptake has most likely to be attributed to uptake on other cold surfaces in the flow reactor.

Atmos. Chem. Phys. Discuss., doi:10.5194/acp-2016-247, 2016
Manuscript under review for journal Atmos. Chem. Phys.
Published: 5 April 2016

Atmospheric Chemistry and Physics Discussions

Reinhardt et al. (2003) reported $\gamma_{NAT}(HNO_3) = 0.165$ in the temperature range 160 to 170 K. They used a slow flow reaction cell coupled with DRIFTS (Diffuse Reflectance Infrared Fourier Transform Spectroscopy) for the detection of adsorbed species and downstream FTIR for the detection of gas phase HNO_3.

Hynes et al. (2002) observed continuous uptake of HNO_3 on water-ice films below 215 K and time dependent uptake above 215 K, with the maximum uptake $\gamma_{ice}(HNO_3)$ decreasing from 0.03 at 215 K down to 0.006 at 235 K. They also observed that the uptake of HCl at 218 K on ice surfaces previously dosed with HNO_3 is reversible. Furthermore, the adsorption of HNO_3 on ice surfaces which contained previously adsorbed HCl indicates that HCl is displaced from surface sites by HNO_3.

In this work, the results for the kinetics of H_2O and HNO_3 gas interacting with solid HNO_3 hydrates will be presented. The independent measurement of the rate of evaporation R_{ev} [molec s^{-1} cm^{-3}] and the accommodation coefficient α of H_2O and HNO_3 on α- and β-NAT substrates is performed using a combination of steady state and real time pulsed valve experiments. Results on the kinetics of HCl on HNO_3 hydrates will also be presented. All experiments reported in this work have been performed using a multidiagnostic stirred flow reactor (SFR), which has been described in detail before (Chiesa and Rossi, 2013; Iannarelli and Rossi, 2014). In addition, all experiments have been performed under strict mass balance control with a knowledge on how many molecules of HNO_3, HCl and H_2O were present in the gas vs. the condensed phase (including the vessel walls) at any given time. These experiments have been described by Iannarelli and Rossi (2015).

2 Experimental Apparatus and Methodology

2.1 Experimental Apparatus and Growth Protocols

Figure 1 shows a schematic of the reactor used in this work with the experimental diagnostic tools and Table 1 reports its characteristic parameters. Briefly, it consists of a low-pressure stainless steel reactor, which may be used under static (all valves closed) or stirred flow (gate valve closed, leak valves open) conditions. We use absolute total pressure measurement and calibrated residual gas mass spectrometry (MS) to monitor the gas phase and FTIR spectroscopy in transmission for the condensed phase. Thin solid films of up to 2 μm thickness are grown on a temperature controlled Si substrate and an average of 8 scans are

Atmos. Chem. Phys. Discuss., doi:10.5194/acp-2016-247, 2016
Manuscript under review for journal Atmos. Chem. Phys.
Published: 5 April 2016

Atmospheric Chemistry and Physics Discussions

recorded at 4 cm^{-1} resolution in the spectral range 700-4000 cm^{-1} at typical total scan time of 45-60 s.

The 1" Si window is the only cold spot in the reactor exposed to admitted gases and therefore the only place where gas condensation occurs. This allows the establishment of a 1:1 correspondence between the thin film composition and the changes in the gas partial pressures in the reactor. Experimental proof of mass balance has previously been reported for this setup (Delval et al., 2003; Chiesa and Rossi, 2013; Iannarelli and Rossi, 2014).

The introduction of HNO_3 in the system forced us to slightly modify the inlet system used previously (Iannarelli and Rossi, 2014) in order to take into account the fact that HNO_3 is an extremely "sticky" molecule that interacts with the internal surfaces of the reservoir vessel of the inlet system as well as with the reactor walls of the SFR (Iannarelli and Rossi, 2015).

Similarly to the case of HCl and H_2O (Iannarelli and Rossi, 2014) we have described the HNO_3 interaction with the reactor walls using a Langmuir adsorption isotherm and determined the concentration of HNO_3 in the ice sample after calibration of HNO_3 following the methodology described in Iannarelli and Rossi (2015). Table 2 reports the values of the fit parameters of the Langmuir adsorption isotherms for all the gases interacting with the stainless steel (SS304) internal surfaces of the SFR. Binary combinations of HNO_3/H_2O and HCl/H_2O have been used to describe the interaction of the acidic probe gas with the vessel walls in the presence of H_2O vapor.

The protocol for the growth of α-NAT, β-NAT and NAD thin films has also been described in Iannarelli and Rossi (2015). Briefly, the protocol for either hydrate always starts with the growth of pure ice: the chamber is backfilled under SFR conditions with water vapor at flow rates between 5×10^{15} and 10^{16} molec s^{-1}, corresponding to a partial pressure of H_2O, $p(H_2O)$ between 4.7 and 9.4×10^{-4} Torr (both apertures open), with the Si substrate held at temperature in the range 167 to 175 K. The pure ice film grows on both sides of the Si substrate to a thickness of typically 1 μm and the H_2O flow is halted (Iannarelli and Rossi, 2014). The temperature of the support is then set to the value used for the growth of the desired HNO_3 hydrate at a typical rate of ±0.3 K min^{-1}.

The growth protocols for α-NAT and NAD are similar and start after the deposition of a pure ice film: the temperature of the Si substrate is held in the range 180 to 185 K for α-NAT and at 168 K for NAD. The sample is exposed for approximately 10 min at SFR conditions to HNO_3 vapor at flow rates in the range 3 to 7×10^{14} molecule s^{-1} for α-NAT and 9×10^{14}

Atmos. Chem. Phys. Discuss., doi:10.5194/acp-2016-247, 2016
Manuscript under review for journal Atmos. Chem. Phys.
Published: 5 April 2016

molecule s^{-1} for NAD. The typical total dose of HNO_3 admitted into the reactor is 2 to 3×10^{17} molecules and 4×10^{17} molecules for α-NAT and NAD, respectively, with almost all of it adsorbed onto the ice film. In both cases, we observe the formation of a new phase after approximately 5 min of exposure as shown in the change of the FTIR absorption spectrum. The present experimental conditions seem to show that no nucleation barrier is present for α-NAT and NAD growth, in agreement with previous works (Hanson, 1992; Middlebrook et al., 1992; Biermann et al., 1998). In contrast, Zondlo et al. (2000) have shown that crystalline growth occurs via an intermediate stage of supercooled H_2O/HNO_3 liquid forming over ice. After exposure the temperature of the substrate is set to the desired value for the kinetic experiments on α-NAT or NAD as a substrate.

The protocol for the growth of β-NAT is different compared to NAD and α-NAT hydrates as it only starts after the growth of an α-NAT film. After the HNO_3 flow has been halted, the α-NAT/ice system is set to static conditions and the temperature increased to 195 K. During the temperature increase the α-NAT film converts to β-NAT as shown by means of FTIR spectroscopy (Koehler et al., 1992; Iannarelli and Rossi, 2015), and once the conversion is completed the temperature is set to the desired value to start the kinetic experiments using β-NAT as substrate. Typical growth protocols under mass balance control showing both the FTIR transmission as well as the corresponding MS signals of HNO_3 as a function of deposition time have been published previously (Iannarelli and Rossi, 2015).

In all samples used for this work, we never have a pure HNO_3 hydrate because we always operate under conditions of excess of ice. Excess ice has been shown to have a stabilizing effect on both α-NAT and β-NAT (Weiss et al., 2016) and in all our experiments the presence of excess ice has been confirmed from FTIR spectra (Iannarelli and Rossi, 2015).

2.2 Experimental Methodology

The experimental methodology used in this work is an extension of the methodology reported in Iannarelli and Rossi (2014) where the combination of real-time pulsed valve and steady state experiments allowed the independent measurement of the rate of evaporation R_{ev} [molec s^{-1} cm^{-3}] and the accommodation coefficient α of HCl and H_2O on crystalline and amorphous HCl hydrates.

For each gas X (X = H_2O, HNO_3, HCl) admitted into the reactor in the presence of ice, the following flow balance equation holds at steady state:

Atmos. Chem. Phys. Discuss., doi:10.5194/acp-2016-247, 2016
Manuscript under review for journal Atmos. Chem. Phys.
Published: 5 April 2016

Atmospheric Chemistry and Physics Discussions

$$F_{in}(X) + F_{des}(X) + F_{ev}(X) = F_{SS}(X) + F_{ads,w}(X) + F_{ads,ice}(X) \quad (1)$$

All terms are flow rates in molec s^{-1}: F_{in} is the flow rate of molecules admitted into the reactor, F_{des} the flow rate of molecules desorbing from the reactor walls, F_{ev} the flow rate of molecules evaporating from the ice surface, F_{SS} the flow rate of molecules effusing through the leak valve into the MS chamber, $F_{ads,w}$ the flow rate of molecules adsorbing onto the reactor walls and $F_{ads,ice}$ the flow rate of molecules adsorbing onto the ice film.

Under the assumption that the adsorption onto the walls may be described as a Langmuir-type adsorption, Eq. (1) may be expressed as follows for a gas X:

$$V \cdot R_{in}(X) + N_{TOT} \cdot k_{des,w}(X) \cdot \theta + V \cdot R_{ev}(X) = \\ = V \cdot R_{SS}(X) + S_w \cdot \frac{\alpha_w(X) \cdot \bar{c}}{4}(1-\theta)\,[X]_{SS} + S_{film} \cdot \frac{\alpha_{film}(X) \cdot \bar{c}}{4}[X]_{SS} \quad (2)$$

where V is the reactor volume in cm^3, $R_{in}(X)$ the rate of molecules X admitted in the chamber in molec·s^{-1}·cm^{-3}, N_{TOT} the total number of molecules X adsorbed onto the reactor walls, $k_{des,w}(X)$ the desorption rate constant from the reactor walls in s^{-1}, θ the fractional surface coverage in terms of a molecular monolayer, $R_{ev}(X)$ the rate of evaporation of X from the ice in molec·s^{-1}·cm^{-3}, $R_{SS}(X)$ the rate of effusion through the leak valve in molec·s^{-1}·cm^{-3}, S_w and S_{film} the surfaces of the reactor walls and the thin film in cm^2, $\alpha_w(X)$ and $\alpha_{film}(X)$ the accommodation coefficients of X on the walls and on the thin film, $[X]_{SS}$ the concentration at steady state in molec cm^{-3} and $\bar{c}$ the mean thermal velocity of a molecule in cm·s^{-1}, respectively. The mathematical derivation of Eq. (2) may be found in Supplement B of Iannarelli and Rossi (2014).

Pulsed valve (PV) experiments and Langmuir adsorption isotherms have been used in order to measure $k_{des,w}(X)$ and $\alpha_w(X)$ (Iannarelli and Rossi, 2014), leaving only two unknown parameters in Eq. (2): $R_{ev}(X)$ and $\alpha_{film}(X)$. The Langmuir adsorption isotherms are shown in Figure S1 of Supplement A whereas the parameters for the best fit are reported in Table 2.

In the case of H_2O, once the selected substrate has been grown according to the protocol briefly described above, the film is set to a chosen temperature. After steady state conditions are established, a series of H_2O pulses are admitted into the reactor. The exponential decay of the MS signal at m/z 18 (k_d) is given by the sum of the measured k_{esc}, the adsorption rate constant on the walls (k_w) and the adsorption rate constant (k_c) onto the ice, namely $k_d = k_{esc} +$

Atmos. Chem. Phys. Discuss., doi:10.5194/acp-2016-247, 2016
Manuscript under review for journal Atmos. Chem. Phys.
Published: 5 April 2016

Atmospheric Chemistry and Physics Discussions

k_w + k_c, in the aftermath of a pulse. The accommodation coefficient $\alpha_{film}(H_2O)$ may be then calculated according to Eq. (3):

$$\alpha_{film}(H_2O) = \frac{k_c(H_2O)}{\omega(H_2O)} \quad (3)$$

where $\omega(H_2O)$ is the calculated gas-surface collision frequency in s^{-1} and is reported in Table 1.

The steady state MS signal established before the pulse series represents the calibrated flow rate of molecules effusing through the leak valve, $F_{SS}(H_2O)$, in Eq. (1) and it may be used to calculate the concentration at steady state $[X]_{SS}$ according to Eq. (4):

$$[X]_{SS} = \frac{F_{SS}(X)}{k_{esc}(X)V} \quad (4)$$

where $k_{esc}(X)$ is the effusion rate constant of gas X out of the reactor in s^{-1} (see Table 1). Finally, $[X]_{SS}$ is used to calculate $R_{ev}(X)$ using Eq. (2).

Subsequently, the film is set to a higher temperature, $F_{SS}(H_2O)$ is recorded and a series of H_2O pulses applied to the same ice sample. This experimental protocol has been repeated for each measured point in the temperature interval of interest.

Under the present experimental conditions, PV experiments of HNO_3 leading to transient supersaturation of HNO_3 are hampered by excessive pulse broadening, most probably owing to the strong adsorption of HNO_3 on ice and the stainless steel vessel walls that makes the observation and interpretation of a HNO_3 pulse difficult for low doses in the presence of ice. In this case the advantage of the PV technique as a real-time method of observation is lost.

Therefore, in order to measure the kinetics of HNO_3 gas in the presence of α-NAT, β-NAT and NAD ice films we have used the two-orifice method first described by Pratte et al. (2006). It has been modified to take into account the interaction of HNO_3 with the internal walls of the SFR. The two-orifice method has also been used to measure the kinetics of H_2O on HNO_3 hydrates in order to compare these results with the results of PV experiments for H_2O.

The two-orifice (TO) method allows the separation of the rate of evaporation $R_{ev}(X)$ and the condensation rate constant $k_c(X)$ of a gas X by choosing two different escape orifices and measuring the corresponding value of concentration $[X]_{SS}$ at steady state of gas X inside the reactor. By alternatively opening the small orifice (S) and both orifices (M) (see Figure 1), two steady state equations hold for a probe gas X which are reported in Eqs. (5) and (6) taking into account the interaction with the reactor walls:

Atmos. Chem. Phys. Discuss., doi:10.5194/acp-2016-247, 2016
Manuscript under review for journal Atmos. Chem. Phys.
Published: 5 April 2016

Atmospheric Chemistry and Physics Discussions

306 $$R_{ev}(X) + \frac{N_{TOT}}{V} \cdot k_{des,w}(X) \cdot \theta = (k_c(X) + k^S_{esc}(X)) \cdot [X]^S_{SS} + \frac{k_w(X)}{V} \cdot (1-\theta) \cdot [X]^S_{SS}$$

307 (5)

308 $$R_{ev}(X) + \frac{N_{TOT}}{V} \cdot k_{des,w}(X) \cdot \theta = (k_c(X) + k^M_{esc}(X)) \cdot [X]^M_{SS} + \frac{k_w(X)}{V} \cdot (1-\theta) \cdot [X]^M_{SS}$$

309 (6)

310 where the superscript indexes indicate small orifice only (S) or both orifices (M) open,
311 respectively.

312 The kinetic parameters $R_{ev}(X)$ and $k_c(X)$ are calculated from Eqs. (7) and (8) as follows:

313 $$k_c(X) = \frac{k^M_{esc}(X) \cdot [X]^M_{SS} - k^S_{esc}(X) \cdot [X]^S_{SS}}{[X]^S_{SS} - [X]^M_{SS}} - k_w(X) \cdot (1-\theta) \quad (7)$$

314 $$R_{ev}(X) = \frac{(k^M_{esc}(X) - k^S_{esc}(X)) \cdot [X]^S_{SS} \cdot [X]^M_{SS}}{[X]^S_{SS} - [X]^M_{SS}} - \frac{N_{TOT}}{V} \cdot k_{des,w}(X) \cdot \theta \quad (8)$$

315 This method leads to larger uncertainties for both $R_{ev}(X)$ and $k_c(X)$ compared to the combined
316 PV and steady state method used before. The reason lies in the fact that two similarly large
317 numbers, namely $[X]^S_{SS}$ and $[X]^M_{SS}$, are subtracted in the denominators of equations Eqs. (7)
318 and (8) leading to an uncertain value of $k_c(X)$ and $R_{ev}(X)$. In other words, the noise in the
319 signal from the MS is such that the two data sets for the small orifice and both orifices open
320 are sometimes insufficiently linearly independent of each other within experimental
321 uncertainty.

322 We also used the combination of real-time PV and steady state experiments using HCl as a
323 probe gas and applied the experimental method described previously in order to measure the
324 kinetics of HCl, R_{ev}(HCl) and α(HCl), in the presence of α-NAT and β-NAT ice films.

325 Once the kinetics $R_{ev}(X)$ and $k_c(X)$ have been measured using the combination of PV and
326 steady state experiments (H_2O, HCl) or the two-orifice method (HNO_3, H_2O), we may
327 calculate the equilibrium vapour pressure $P_{eq}(X)$ for each gas according to Eq. (9):

328 $$P_{eq}(X) = \frac{R_{ev}(X)}{k_c(X)} \cdot \frac{RT}{N_A} \quad (9)$$

329 where R is the molar gas constant in cm^3 Torr K^{-1} mol^{-1}, T the temperature of the thin film in
330 K and N_A Avogadro's constant in molec mol^{-1}.

Atmos. Chem. Phys. Discuss., doi:10.5194/acp-2016-247, 2016
Manuscript under review for journal Atmos. Chem. Phys.
Published: 5 April 2016

Atmospheric Chemistry and Physics Discussions

3 Results

3.1 Crystalline α-NAT Thin Films

The kinetic results for the heterogeneous interaction of H_2O and HNO_3 with α-NAT and NAD thin films obtained in PV and TO experiments are displayed in Figure 2. Full symbols represent PV experiments: full red circles correspond to experiments on α-NAT substrates, and full green squares to experiments on NAD substrates. Empty symbols represent TO experiments with red circles representing H_2O and black triangles HNO_3 results. Pure ice experiments are displayed as inverse blue triangles for comparison purposes. The calculated relative error for PV experiments is 30% whereas for TO experiments we estimate a relative error of 60%.

Figure 2a shows the measured accommodation coefficients $\alpha_{\alpha-NAT}(X)$, (X = H_2O, HNO_3), as a function of temperature. $\alpha_{\alpha-NAT}(H_2O)$ in PV experiments (full red circles) decreases as a function of temperature in the range 167-188.5 K, varying from 0.08 at 167 K to 3.1×10^{-3} at 188.5 K, which is a factor of 30 lower than $\alpha_{ice}(H_2O)$ on pure ice at the same temperature. The scatter in the data is not an artifact and is due to the sample-to-sample variability of the crystalline samples we use and the randomness of the crystalline nucleation process. The variability may be in surface composition, morphology and smoothness as shown in previous studies (McNeill et al., 2007; Iannarelli and Rossi, 2014).

$\alpha_{\alpha-NAT}(H_2O)$ in TO experiments (empty red circles) yields different results. For temperatures lower than 185 K it is equal to $\alpha_{\alpha-NAT}(H_2O)$ on α-NAT in PV experiments within experimental error. For temperatures higher than 185 K $\alpha_{\alpha-NAT}(H_2O)$ increases as a function of temperature in contrast to results of PV experiments (full red circles) varying from 8×10^{-3} at 183 K to 0.08 at 193.5 K, being equal to $\alpha_{ice}(H_2O)$ on pure ice within experimental error at the highest temperature. This result compares favorably with the results of Delval and Rossi (2005) which showed a positive temperature dependence of $\alpha_{\alpha-NAT}(H_2O)$ in the temperature range 182-207 K. $\alpha_{NAD}(H_2O)$ in PV experiments (green full squares) is equal within experimental error to $\alpha_{\alpha-NAT}(H_2O)$.

$\alpha_{\alpha-NAT}(HNO_3)$ (black empty triangles) increases as a function of temperature in the measured temperature range from a value of approximately 0.005 at 181 K to a value of 0.13 at 188 K. The narrow temperature range follows from the high uncertainties of the two-orifice method at low temperatures and the increasingly rapid conversion of α-NAT to β-NAT at high

Atmos. Chem. Phys. Discuss., doi:10.5194/acp-2016-247, 2016
Manuscript under review for journal Atmos. Chem. Phys.
Published: 5 April 2016

362 temperatures. These values are lower by a factor of 2 to 40 compared to the preferred values
363 indicated by the IUPAC Subcommittee on Gas Kinetic Data Evaluation (Crowley et al.,
364 2010).

365 Figure 2b shows results for the rate of evaporation $R_{ev}(X)$ in molec s^{-1} cm^{-3} as a function of
366 temperature. The same symbols as for panel (a) are used. $R_{ev}(H_2O)$ on α-NAT in PV
367 experiments is lower by a factor of 2 compared to $R_{ev}(H_2O)$ on pure ice at temperatures lower
368 than 175 K. For temperatures higher than 175 K, $R_{ev}(H_2O)$ on α-NAT is lower on average by
369 up to a factor of 50 compared to $R_{ev}(H_2O)$ on pure ice. This result is very different compared
370 to the case of HCl where the evaporation of H_2O takes place at a rate characteristic of pure ice
371 despite the presence of adsorbed HCl on the ice and is in agreement with the findings of
372 Delval and Rossi (2005).

373 $R_{ev}(H_2O)$ on α-NAT measured using the TO method is equal within experimental error to
374 $R_{ev}(H_2O)$ obtained in PV experiments. $R_{ev}(H_2O)$ on NAD is equal to within experimental
375 error to $R_{ev}(H_2O)$ on α-NAT. The full black line shows the rate of evaporation of pure water
376 for the system in use, calculated from literature results of the equilibrium vapor pressure
377 (Marti and Mauersberger, 1993) using $\alpha = 1$, whereas the dashed black line represents
378 extrapolated values of $R_{ev}(H_2O)$ for temperatures lower than 173 K using the expression
379 provided by Mauersberger and coworkers (Marti and Mauersberger, 1993; Mauersberger and
380 Krankowsky, 2003).

381 Figure 2c shows the results for $P_{eq}(X)$ in Torr calculated according to Eq. (9) for both H_2O
382 and HNO_3 as a function of temperature. The same symbols as in panels (a) and (b) are used.
383 $P_{eq}(H_2O)$ of α-NAT calculated from the kinetic parameters measured in PV experiments is
384 lower by a factor of approximately 3 compared to $P_{eq}(H_2O)$ on pure ice at temperatures higher
385 than 180 K. For temperatures lower than 180 K $P_{eq}(H_2O)$ of α-NAT is close to $P_{eq}(H_2O)$ of
386 pure ice because the present samples are water-rich (Molina, 1994) with a HNO_3 mole
387 fraction of less than 10%.

388 $P_{eq}(H_2O)$ of α-NAT calculated from the results of TO experiments is lower by up to a factor
389 of 10 compared to $P_{eq}(H_2O)$ of pure ice in the temperature range 180-193.5 K. At
390 temperatures lower than 180 K, $P_{eq}(H_2O)$ of α-NAT from TO experiments is equal within
391 experimental error to $P_{eq}(H_2O)$ of α-NAT in PV experiments. $P_{eq}(HNO_3)$ of α-NAT is lower
392 by a factor of 1000 in the temperature range 181-188 K compared to $P_{eq}(H_2O)$ on pure ice.

Atmos. Chem. Phys. Discuss., doi:10.5194/acp-2016-247, 2016
Manuscript under review for journal Atmos. Chem. Phys.
Published: 5 April 2016

393 The values obtained for the equilibrium vapor pressure have been compared with the
394 HNO_3/H_2O phase diagram constructed by McElroy et al. (1986); Hamill et al. (1988); Molina
395 (1994). Figure 3 shows the results for α-NAT and metastable NAD films, PV and TO
396 experiments. The solid lines represent the coexistence conditions for two phases and the
397 dashed lines represent vapor pressures of liquids with composition given as % (w/w) of
398 HNO_3. The shaded rectangular area represents typical polar stratospheric conditions. The
399 slope m of the coexistence lines depends on the difference of the enthalpies of sublimation of
400 the two acid hydrate species, namely NAM and NAT, according to Eq. (10) (Wooldridge et
401 al., 1995):

402 $$m = \frac{\Delta H^1_{subl} - \Delta H^2_{subl}}{(n_1 - n_2)\,R} \qquad (10)$$

403 where ΔH^1_{subl} and ΔH^2_{subl} are the enthalpies of sublimation of the acid hydrates in kJ/mol, n_1
404 and n_2 the number of water molecules of the respective hydrate and R is the gas constant in J
405 mol^{-1} K^{-1}. The slope of the ice/NAT coexistence line is calculated from Wooldridge et al.
406 (1995) as $m_{ice/NAT}$ = (50.9 kJ/mol)/R and the slope of the NAT/NAM coexistence line is
407 calculated as $m_{NAT/NAM}$ = (55.9 kJ/mol)/R.

408 All α-NAT experiments lie in the existence area of nitric acid trihydrate, as expected. On the
409 other hand, α-NAT under polar stratospheric conditions (shaded rectangular area) is unstable
410 and starts to convert into the stable β-NAT phase (Koehler et al., 1992). The small number of
411 α-NAT samples we reported in the shaded gray area is further confirmation of results reported
412 in the literature. NAD samples are expected to lie closer to the monohydrate region, given
413 their composition close to the H_2O:HNO_3 = 2:1 stoichiometry (Iannarelli and Rossi, 2015).
414 Nevertheless, the pure ice phase is still dominant in our samples and all our samples are
415 water-rich (Molina, 1994) with a HNO_3 mole fraction, even in NAD films, of less than 10%.

416 ### 3.2 Crystalline β-NAT Thin Films

417 The results for β-NAT thin films obtained in PV and TO experiments are displayed in Figure
418 4. Full and empty red squares represent PV and TO experiments, respectively, with red
419 squares representing H_2O and black triangles HNO_3 results. Pure ice experiments are
420 displayed as inverse blue triangles for comparison. The calculated relative error for PV
421 experiments is 30% whereas for TO experiments we estimate a relative error of 60%.

Atmos. Chem. Phys. Discuss., doi:10.5194/acp-2016-247, 2016
Manuscript under review for journal Atmos. Chem. Phys.
Published: 5 April 2016

Atmospheric Chemistry and Physics Discussions

Figure 4a shows the measured $\alpha_{\beta-NAT}(X)$ as a function of temperature. $\alpha_{\beta-NAT}(H_2O)$ in PV experiments (full red squares) shows scatter similar to the case of $\alpha_{HH}(HCl)$ on crystalline HCl hexahydrate (Iannarelli and Rossi, 2014). Also in this case, a variation of up to a factor of 10 for results at the same temperature is observed. We may interpret this result like in the HCl hexahydrate case where the scatter may be caused by the variability of the surface composition, the morphology or the smoothness of the ice surface (McNeill et al., 2007). Similar results have recently been presented by Moussa et al. (2013) regarding the nitric acid-induced surface disorder on ice. In any case, all results show that $\alpha_{\beta-NAT}(H_2O)$ is at least a factor of 10 lower than $\alpha_{ice}(H_2O)$ on pure ice in the temperature range 182-200 K.

$\alpha_{\beta-NAT}(H_2O)$ in TO experiments (empty red squares) on the other hand, increases as a function of temperature in the temperature range 182-198 K varying from 0.013 at 182 K to approximately 0.1 at 198 K, being equal at the highest temperature to $\alpha_{ice}(H_2O)$ on pure ice within experimental error. This result is in contrast to Delval and Rossi (2005) who report a negative temperature dependence of $\alpha_{\beta-NAT}(H_2O)$ in the temperature range 182-207 K. A possible reasons for the different behavior of PV and TO experiments may be intrinsic in the nature of PV experiments: the ice surface is exposed to a series of pulses of H_2O and the free sites may be saturated before the introduction of each consecutive pulse. We suspect this may be the reason for the discrepancy between PV and TO experiments and we will consider the results of TO experiments as the preferred values of this work despite the larger experimental scatter.

Like $\alpha_{\beta-NAT}(H_2O)$, the values of $\alpha_{\beta-NAT}(HNO_3)$ (black empty triangles) increase as a function of temperature in the measured temperature range from a value of approximately 0.015 at 182 K to a value of 0.08 at 195.5 K. However, the values have a large estimated uncertainty. These values are lower by a factor of 2 to 10 compared to the preferred values indicated by the IUPAC Subcommittee on Gas Kinetic Data Evaluation (Crowley et al., 2010) in the temperature range 190 to 200 K.

Figure 4b shows results for $R_{ev}(X)$ in molec s^{-1} cm^{-3} as a function of temperature. The same symbols as in panel (a) are used. $R_{ev}(H_2O)$ on β-NAT in PV experiments is lower by a factor of 50 compared to $R_{ev}(H_2O)$ on pure ice in the temperature range 182-200 K. As in the case of α-NAT, this result is very different compared to the case of HCl where the evaporation of H_2O is not influenced by the presence of adsorbed HCl on the ice and takes place at a rate characteristic of pure ice for all HCl concentrations used.

Atmos. Chem. Phys. Discuss., doi:10.5194/acp-2016-247, 2016
Manuscript under review for journal Atmos. Chem. Phys.
Published: 5 April 2016

454 $R_{ev}(H_2O)$ on β-NAT measured using the TO method is close to $R_{ev}(H_2O)$ obtained in PV
455 experiments, the former being approximately a factor of 2 higher. $R_{ev}(HNO_3)$ on β-NAT
456 increases in the temperature range 182-195.5 K with a steeper slope compared to $R_{ev}(H_2O)$,
457 the former being smaller by approximately a factor of 1000 at low and 50 at higher
458 temperature compared to $R_{ev}(H_2O)$ of β-NAT. It varies from 2×10^{8} at 182 K to 8.5×10^{9} molec
459 s^{-1} cm^{-3} at 195.5 K.

460 Figure 4c shows the results for $P_{eq}(X)$ in Torr calculated according to Eq. (9) for both H_2O
461 and HNO_3 as a function of temperature. The same symbols as in panels (a) and (b) are used.
462 $P_{eq}(H_2O)$ of β-NAT calculated from the results of TO experiments is lower by up to a factor
463 of 10 in the middle of the covered T-range compared to $P_{eq}(H_2O)$ of pure ice in the
464 temperature range 182-195.5 K. $P_{eq}(H_2O)$ of β-NAT calculated from the kinetic parameters
465 measured in PV agrees with TO experiments within experimental uncertainty. Saturation
466 effects in PV experiments will affect both the accommodation (α) and evaporation (J_{ev})
467 process to the same extent such that P_{eq} should be invariant to the chosen experimental
468 procedure (PV or TO).

469 The scatter of $P_{eq}(H_2O)$ is of the same magnitude as the scatter of $\alpha_{\beta-NAT}(H_2O)$ and may
470 likewise be explained by an increase in the substrate roughness or inhomogeneous nature of
471 the β-NAT surface owing to exposure to repetitive transient saturation of H_2O in the
472 aftermath of each pulse.

473 Figure 5 shows the HNO_3/H_2O phase diagram with the results obtained for β-NAT films: all
474 β-NAT experiments lie in the existence area of nitric acid trihydrate and the majority of points
475 are in the rectangular shaded area representing polar stratospheric conditions. As already
476 mentioned, β-NAT is the stable phase under these conditions and our results agree well with
477 the literature (McElroy et al., 1986; Hamill et al., 1988; Molina, 1994; Koehler et al., 1992).

478 3.3 HCl kinetics on α-NAT and β-NAT Thin Films

479 As already mentioned, we used a combination of real-time PV and steady state experiments
480 using HCl as probing gas in order to measure the kinetics of HCl interacting with α-NAT and
481 β-NAT ice films.

482 The current experimental setup does not allow the measurement of the kinetics of 3 gases at
483 the same time. We therefore had to make some assumptions and/or simplifications in order to

Atmos. Chem. Phys. Discuss., doi:10.5194/acp-2016-247, 2016
Manuscript under review for journal Atmos. Chem. Phys.
Published: 5 April 2016

484 measure the unknown parameters of Eq. (2) for each gas used. Specifically, we made the
485 following assumptions, both for α-NAT and β-NAT substrates:

486 • $R_{ev}(H_2O)$ on NAT remains unchanged in the presence of HCl
487 • $\alpha_{NAT}(H_2O)$ remains unchanged in the presence of HCl
488 • $\alpha_{NAT}(HNO_3)$ remains unchanged in the presence of HCl

489 Under these assumptions, no additional measurements of the heterogeneous kinetics of H_2O
490 in the presence of HCl have been performed. We have measured the steady-state flow
491 $F_{SS}(HNO_3)$ before each HCl pulse series and used previously measured $\alpha_{\alpha-NAT}(HNO_3)$ and
492 $\alpha_{\beta-NAT}(HNO_3)$ from TO experiments on α-NAT and β-NAT phases in order to calculate
493 $R_{ev}(HNO_3)$ and $P_{eq}(HNO_3)$ according to Eqs. (8) and (9) in HCl-PV experiments as well. As a
494 net result we measure or calculate the following kinetic parameters for α-NAT and β-NAT
495 substrates: $R_{ev}(HCl)$, $\alpha_{NAT}(HCl)$ and $R_{ev}(HNO_3)$ in the presence of HCl.

496 Figure 6 displays the results of HCl-PV experiments on α-NAT substrates. Full red diamonds
497 represent the results for HCl whereas full black circles represent HNO_3 results using
498 $\alpha_{\alpha-NAT}(HNO_3)$ from TO experiments and $F_{SS}(HNO_3)$ from HCl-PV experiments. Empty
499 black triangles represent results for HNO_3 in TO experiments reported from Figure 2 for
500 comparison.

501 Figure 6a displays the measured $\alpha_{\alpha-NAT}(X)$ as a function of temperature. $\alpha_{\alpha-NAT}(HCl)$ (full
502 red diamonds) slightly decreases as a function of temperature in the range 177.5-199.5 K,
503 being equal to $\alpha_{ice}(H_2O)$ on pure ice at low temperatures and lower by a factor of 4 at T =
504 199.5 K. Values of $\alpha_{\alpha-NAT}(HNO_3)$ measured in TO experiments in the absence of HCl are
505 reported as empty black triangles. We used these values in order to calculate $R_{ev}(HNO_3)$ and
506 $P_{eq}(HNO_3)$ in the presence of HCl.

507 Figure 6b shows results for $R_{ev}(X)$ in molec s^{-1} cm^{-3} as a function of temperature. The same
508 symbols as in panel (a) are used. $R_{ev}(HCl)$ on α-NAT slightly increases as a function of
509 temperature and is lower by a factor of 1000 in the measured temperature range 177.5-199.5
510 K compared to $R_{ev}(H_2O)$ on pure ice. $R_{ev}(HNO_3)$ increases as a function of temperature,
511 varying from 1×10^8 at 181 K to 9×10^9 molec s^{-1} cm^{-3} at 189 K. The presence of HCl does not
512 have any effect on the rate of evaporation of HNO_3 from α-NAT films: we observe no
513 increase of $F_{ss}(HNO_3)$ following HCl pulses and $R_{ev}(HNO_3)$ in the presence of adsorbed HCl
514 molecules (full black circles) is identical within experimental error to $R_{ev}(HNO_3)$ of α-NAT

Atmos. Chem. Phys. Discuss., doi:10.5194/acp-2016-247, 2016
Manuscript under review for journal Atmos. Chem. Phys.
Published: 5 April 2016

Atmospheric Chemistry and Physics Discussions

films free of adsorbed HCl (empty black triangles). However, this result is contingent upon the assumptions listed before, namely $\alpha_{\alpha-NAT}(HNO_3)$ being independent of the presence or absence of HCl.

Figure 6c shows the results for $P_{eq}(X)$ in Torr calculated according to Eq. (9) for both HCl and HNO_3 as a function of temperature. The same symbols as in panel (a) and (b) are used. $P_{eq}(HCl)$ of α-NAT is lower by a factor of approximately 100 compared to $P_{eq}(H_2O)$ on pure ice in the measured temperature range. A comparison with the results of $P_{eq}(HCl)$ of crystalline HCl hexahydrate and amorphous HCl/H_2O mixtures calculated using the same experimental methodology (Iannarelli and Rossi, 2014) shows that $P_{eq}(HCl)$ of α-NAT is lower by a factor of approximately 10 compare to $P_{eq}(HCl)$ of crystalline hexahydrate in the overlapping temperature range (177.5-193.5 K).

$P_{eq}(HCl)$ of amorphous HCl/H_2O mixtures is higher by a factor of 20 compared to $P_{eq}(HCl)$ of α-NAT at low temperatures (177.5 K) with the difference decreasing at high temperatures (199.5 K) where $P_{eq}(HCl)$ of the amorphous mixture is only a factor of 4 higher than $P_{eq}(HCl)$ of α-NAT.

$P_{eq}(HNO_3)$ on HCl-doped α-NAT films is equal within experimental error to $P_{eq}(HNO_3)$ of α-NAT films free of adsorbed HCl. It is lower by a factor of 1000 compared to $P_{eq}(H_2O)$ on pure ice in the measured temperature range 177.5-199.5 K.

Figure 7a (symbols have the same meaning as in Figure 6) shows the measured values of $\alpha_{\beta-NAT}(X)$ as a function of temperature. $\alpha_{\beta-NAT}(HCl)$ slightly decreases as a function of temperature in the range 177-201 K, varying from 0.025 at 177 K to 0.016 at 201 K. As for the case of α-NAT, we assume that $\alpha_{\beta-NAT}(HNO_3)$ (empty black triangles) equals the measured values of $\alpha_{\beta-NAT}(HNO_3)$ on HCl-free β-NAT in two-orifice experiments whose results are displayed in Figure 4a.

Figure 7b shows results for the $R_{ev}(X)$ in molec s^{-1} cm^{-3} as a function of temperature. The same symbols as in Panel (a) are used. $R_{ev}(HCl)$ on β-NAT is equal at higher temperature within experimental uncertainty to $R_{ev}(HCl)$ on α-NAT and is lower by a factor of 1000 in the temperature range 177- 201 K compared to $R_{ev}(H_2O)$ on pure ice. $R_{ev}(HNO_3)$ on HCl-doped β-NAT films, being equal within experimental error to $R_{ev}(HNO_3)$ of undoped β-NAT films, indicates that adsorbed HCl molecules seem to have no effect on the rate of evaporation of HNO_3 from β-NAT films in the presence of HCl as well.

Atmos. Chem. Phys. Discuss., doi:10.5194/acp-2016-247, 2016
Manuscript under review for journal Atmos. Chem. Phys.
Published: 5 April 2016

Atmospheric Chemistry and Physics Discussions

Figure 7c shows the results for $P_{eq}(X)$ in Torr calculated according to Eq. (9) for both HCl and HNO_3 as a function of temperature. The same symbols as in panel (a) and (b) are used. $P_{eq}(HCl)$ of β-NAT is lower by a factor of approximately 100 compared to $P_{eq}(H_2O)$ on pure ice. $P_{eq}(HCl)$ of β-NAT is identical within experimental uncertainty to $P_{eq}(HCl)$ of α-NAT in the measured temperature range 177-201 K and the same observations are valid when comparing $P_{eq}(HCl)$ of crystalline HCl hexahydrate with amorphous HCl/H_2O mixtures (Iannarelli and Rossi, 2014).

4 Discussion

In this work we have been able to grow HNO_3 hydrates at temperatures relevant to the stratosphere with tight control on the deposition conditions whose details have been published by Iannarelli and Rossi (2015) as far as the mass balance is concerned. Direct crystallization of α-NAT film on pure ice has been observed upon HNO_3 deposition. Under the present system conditions β-NAT was never observed to crystallize directly upon HNO_3 deposition but was always obtained as the stable form after conversion of α-NAT films. Temperatures higher than 185 K are necessary for the conversion to occur on the time scale of the experiments we have performed.

$\alpha_{\alpha-NAT}(H_2O)$ shows two distinct temperature dependent regimes. At temperatures lower than 180-185 K it decreases as a function of temperature reaching a minimum of approximately 0.003 at 185 K as displayed in Figure 2a. For temperatures higher than 185 K, $\alpha_{\alpha-NAT}(H_2O)$ increases as a function of temperature, being equal to $\alpha_{ice}(H_2O)$ on pure ice and $\alpha_{\beta-NAT}(H_2O)$ at 193.5 K. An Arrhenius representation of the evaporative flux $J_{ev}(H_2O)$ (see Table 1) on α-NAT shows two distinct regimes of temperature dependence, as well. Figure 8 reports the results for PV and TO experiments as full and empty red circles, respectively. We keep the two data sets separated for clarity, but the results of PV and TO experiments are indistinguishable within experimental uncertainty in the measured temperature range.

Eqs. (11) and (12) present the two-parameter representations of the Arrhenius lines for $J_{ev}(H_2O)$ displayed in Figure 8. Equations (11) and (12) represent the solid and dashed red lines, respectively, with R = 8.314 J K^{-1} mol^{-1} used throughout:

$$181\ K \leq T \leq 193.5\ K:\ \log J_{ev}(H_2O)[molec \cdot cm^{-2} \cdot s^{-1}] = (35.9 \pm 2.8) - \frac{(75.3 \pm 9.9)\times 10^3}{2.303\ RT} \quad (11)$$

Atmos. Chem. Phys. Discuss., doi:10.5194/acp-2016-247, 2016
Manuscript under review for journal Atmos. Chem. Phys.
Published: 5 April 2016

Atmospheric Chemistry and Physics Discussions

$$167\ \mathrm{K} \leq \mathrm{T} \leq 181\ \mathrm{K}: \log \mathrm{J_{ev}(H_2O)[molec \cdot cm^{-2} \cdot s^{-1}]} = (15.1 \pm 1.2) - \frac{(3.5 \pm 4.2)\times 10^3}{2.303\ \mathrm{RT}} \quad (12)$$

Table 3 reports a synopsis of the kinetic (J_{ev}) as well as the thermodynamic (P_{eq}) parameters calculated for all experiments of the present work.

The considerable scatter in the data, reflected in the significant uncertainties of Eqs. (11) and (12), may be explained by the variability of the surface composition of the film as well as the surface roughness and surface disorder of the ice substrates, in analogy to the HCl case (Iannarelli and Rossi, 2014). For HCl the scatter in the kinetic data was thought to be due to the stochastic nature of crystal growth of hexahydrate films compared to amorphous mixtures of HCl/H_2O of similar composition and does not represent a lack of reproducibility.

Moussa et al. (2013) have observed variations of up to a factor of 10 of the HNO_3 vapor pressure of "smooth" ice samples exposed to HNO_3 as a result of induced surface disorder. The exposure of the present samples to repeated high H_2O supersaturation during PV experiments may lead to surface increased disorder due to liquefaction and/or reconstruction. In the high temperature regime we calculate an activation energy for H_2O evaporation $E_{ev}(H_2O)$ = (75.3 ± 9.9) kJ mol^{-1}, and in the low temperature regimes almost no temperature dependence is observed with an activation energy for H_2O evaporation of $E_{ev}(H_2O)$ = (3.5 ± 4.2) kJ mol^{-1}.

The discontinuity in the Arrhenius representation of kinetic parameters has already been observed in pure ice as reported by Chaix et al. (1998); Delval et al. (2003); Delval and Rossi (2004); Pratte et al. (2006). The temperatures at which the discontinuity occurs are higher in previous work: Delval et al. (2003) reported a discontinuity at approximately 208 K in their work on H_2O evaporation from HCl and HBr doped ice substrates. In a quartz crystal microbalance study of H_2O evaporation from pure ice the change in slope is reported at 193 ± 2 K (Delval and Rossi, 2004) comparable with the temperature of 188 ± 2 K reported by Pratte et al. (2006) in their work on the kinetics of H_2O evaporation and condensation on different types of ice.

No clear explanation for this break has yet been advanced. The discontinuity may be an indication of the formation of a new disordered structure similar to the quasi-liquid layer induced by HCl as proposed by McNeill et al. (2006). The observation of the break in pure ice samples as well, however, strongly suggests that the onset of a quasi-liquid layer may be independent of the presence of HCl and that the history and evolution of the sample play a role in the arrangement of the structure, similarly to the case of the presence of cubic ice at

Atmos. Chem. Phys. Discuss., doi:10.5194/acp-2016-247, 2016
Manuscript under review for journal Atmos. Chem. Phys.
Published: 5 April 2016

Atmospheric Chemistry and Physics Discussions

high temperature in common hexagonal ice that finally turned out to be a perturbed hexagonal ice structure (Kuhs et al., 2012).

In the case of β-NAT we have good agreement between PV (dotted line) and TO (solid line) experiments of $P_{eq}(H_2O)$ as shown in the van 't Hoff representation displayed in Figure 9.

As already mentioned, the ice surface is exposed to a series of pulses of H_2O during PV experiments. The free sites may be saturated before the introduction of each consecutive pulse resulting in the discrepancy between PV and TO experiments. We therefore believe that the results from PV experiments are more precise but less accurate owing to partial surface saturation whereas the TO experiments are less precise but more accurate. We chose the latter as the preferred values of this work despite the larger scatter in the data compared to the PV experiments.

Eqs. (13) and (14) reports the best linear fit for TO and PV experiments displayed in Figure 9, respectively:

$$\log P_{ev}(H_2O)[\text{Torr}] = (16.7 \pm 4.9) - \frac{(76.7 \pm 17.7)\times 10^3}{2.303\ RT} \qquad \text{TO – Preferred} \qquad (13)$$

$$\log P_{ev}(H_2O)[\text{Torr}] = (16.7 \pm 3.0) - \frac{(75.5 \pm 11.1)\times 10^3}{2.303\ RT} \qquad \text{PV} \qquad (14)$$

The enthalpies of evaporation of H_2O on β-NAT films calculated for the two measurement techniques are $\Delta H^0_{ev,TO}(H_2O)$ = (76.7 ± 17.7) kJ mol^{-1} for TO and $\Delta H^0_{ev,PV}(H_2O)$ = (75.5 ± 11.1) kJ mol^{-1} for PV experiments, respectively. The results show good agreement between the two experimental techniques despite the experimental scatter. The average value of $\Delta H^0_{ev}(H_2O)$ = (76.1 ± 14.4) kJ mol^{-1} is slightly higher, as expected, but not significantly different compared to α-NAT films. Figure S2 of Supplement C displays a van't Hoff plot for α-NAT with $\Delta H^0_{ev}(H_2O)$ = (70.3 ± 14.1) and (56 ± 5.1) kJ mol^{-1} for TO and PV experiments, respectively. Both values are identical within experimental uncertainty whose average yields $\Delta H^0_{ev}(H_2O)$ = (63.4 ± 9.6) kJ mol^{-1} and which leads to a standard enthalpy of formation slightly larger than that for β-NAT, as expected.

However, we do not have good agreement between TO and PV experiments for the kinetic parameters of β-NAT: a discrepancy is observed in the results of the two measurement techniques regarding $R_{ev}(H_2O)$ and $\alpha(H_2O)$ for β-NAT. Figure 4 already shows a discrepancy in $\alpha(H_2O)$ (full and empty red squares in panel a) with the results of TO experiments being larger by a factor of approximately 5 at 185 K increasing to a factor of 100 at 200 K compared

Atmos. Chem. Phys. Discuss., doi:10.5194/acp-2016-247, 2016
Manuscript under review for journal Atmos. Chem. Phys.
Published: 5 April 2016

to PV experimental results across the whole temperature range. The same qualitative trend, albeit to a smaller extent, is observed for $R_{ev}(H_2O)$ (Figure 4b) and the Arrhenius representation of $J_{ev}(H_2O)$ on β-NAT clearly shows the discrepancy between the different measurement techniques.

The two-parameter representations of the Arrhenius lines displayed in Figure 10 are reported in Eqs. (15) and (16) for TO (solid line) and PV (dotted line) experiments, respectively:

$$\log J_{ev}(H_2O)[\text{molec}\cdot\text{cm}^{-2}\cdot\text{s}^{-1}] = (36.0 \pm 1.3) - \frac{(77.0 \pm 4.9)\times 10^3}{2.303\ \text{RT}} \quad \text{TO – Preferred} \qquad (15)$$

$$\log J_{ev}(H_2O)[\text{molec}\cdot\text{cm}^{-2}\cdot\text{s}^{-1}] = (28.7 \pm 0.7) - \frac{(52.1 \pm 2.4)\times 10^3}{2.303\ \text{RT}} \quad \text{PV} \qquad (16)$$

Contrary to the case of α-NAT, no discontinuity in $J_{ev}(H_2O)$ has been observed in the Arrhenius plot of β-NAT displayed in Figure 10. We attribute the discrepancy between PV and TO experiments to the fact that the former may be subject to partial saturation of uptake and evaporation in the aftermath of transient supersaturation (PV). A look at the results of $\alpha_{\alpha-NAT}(H_2O)$ in Figure 2a reveals that the results of the TO measurement technique agrees well with the PV technique in the overlapping temperature range. However, this plot displays a "hole" of a factor of 20 centered around T = 180 ± 3 K with respect to the values at the fringes of the temperature interval. There are indications that PV experiments on α-NAT substrates may yield lower values of $\alpha_{\alpha-NAT}(H_2O)$ at high temperatures in excess of approximately 182 K (Figure 2a), similarly to the results for $\alpha_{\beta-NAT}(H_2O)$ for a β-NAT film (Figure 4a). This might be an indication that PV experiments are very sensitive to the interfacial nature of the sample. In other words, transient supersaturation (PV) and "passive" steady-state (TO) experiments may address different properties of the gas-condensed surface interface. This is the first time such a large discrepancy between two kinetic measurements techniques has been observed. As expected, thermodynamic results are not affected for reasons of microscopic reversibility because both forward ($\alpha(H_2O)$) and reverse reactions ($J_{ev}(H_2O)$) are affected to the same extent which cancels out for the calculation of the values of thermodynamic parameters.

Figure S3 of Supplement C shows the results of PV experiments using H_2O as a probe gas on α-NAT and β-NAT substrates. Red and black circles represent the decay of series of two pulses on α- and β-NAT, respectively, with the first and second pulse labeled accordingly. In the case of α-NAT films (red circles), the decay of the second pulses is equal to within 20-

Atmos. Chem. Phys. Discuss., doi:10.5194/acp-2016-247, 2016
Manuscript under review for journal Atmos. Chem. Phys.
Published: 5 April 2016

30% of the decay of the initial pulses, and only in a few cases at temperatures higher than 180 K is the decay of the second pulse significantly slower than the initial pulse. In the case of β-NAT films, the decay of second pulses is consistently slower than the decay of first pulses in most cases. This indicates that the surface of β-NAT films exposed to a transient supersaturation of H_2O vapor is more prone to saturation compared to α-NAT.

As mentioned before, we consider the results of TO experiments as preferred for this work despite the larger uncertainty. The enthalpies of evaporation $\Delta H^0_{ev,TO}(H_2O)$ = (76.7 ± 17.7) kJ mol^{-1} and the activation energy for evaporation $E_{ev}(H_2O)$ = (77.0 ± 4.9) kJ mol^{-1} are equal to within experimental uncertainties. We calculate an activation energy of accommodation for H_2O on β-NAT of $E_{acc}(H_2O) = E_{ev}(H_2O) - \Delta H^0_{ev,TO}(H_2O) = 0$. Therefore, no activation energy is required for the accommodation process of H_2O on β-NAT which is an expected experimental outcome. In contrast, the activation energy for H_2O accommodation on α-NAT is computed as $E_{acc}(H_2O) = E_{ev}(H_2O) - \Delta H^0_{ev,average}(H_2O)$ = 75.3 – 63.4 = 11.9 kJ/mol when using a value averaged over the PV and TO experiment of 63.4 kJ/mol for $\Delta H^0_{ev,average}(H_2O)$. This small, but possibly significant positive activation energy is consistent with the temperature dependence of $\alpha_{\beta-NAT}(H_2O)$ displayed in Figure 4a for the TO experiment.

$R_{ev}(H_2O)$ on both α-NAT and β-NAT is smaller compared to $R_{ev}(H_2O)$ on pure ice. This is in agreement with the results of Tolbert and Middlebrook (1990) and Delval and Rossi (2005) who showed that ice coated with a layer of NAT evaporates at a slower rate than pure ice. On the other hand, our results are in contrast with the findings of Biermann et al. (1998) who report that no significant decrease of the H_2O evaporation rate was observed in HNO_3-doped ice films. The discrepancy may be due to the low HNO_3 concentration used by Biermann et al. (1998) compared to our experimental conditions as well as probable wall losses due to HNO_3-wall interaction which was not taken into account in contrast to the present approach .

Delval and Rossi (2005) report that the initial evaporation of H_2O in their experiments was always that of pure ice and that $R_{ev}(H_2O)$ gradually decreases with the evaporation of excess H_2O and the increase in the average HNO_3 mole fraction. They refer to this difference as "high and low evaporation rate" regime of H_2O.

Our observation is somewhat different: $R_{ev}(H_2O)$ on α-NAT and β-NAT is smaller compared to $R_{ev}(H_2O)$ on pure ice over the whole temperature range and for all samples. The reason lies in the fact that the average mole fraction of HNO_3 of the present samples is higher by at least

Atmos. Chem. Phys. Discuss., doi:10.5194/acp-2016-247, 2016
Manuscript under review for journal Atmos. Chem. Phys.
Published: 5 April 2016

Atmospheric Chemistry and Physics Discussions

a factor of 10 compared to the one used by Delval and Rossi (2005). Therefore all our samples are in the "low evaporation rate" regime of H_2O and our results compare well with the results of Delval and Rossi (2005) once they evaporate excess H_2O and reach the "low evaporation rate" regime.

Figure 11 displays both the Arrhenius plots of $J_{ev}(HNO_3)$ (A) and the van 't Hoff plots of $P_{eq}(HNO_3)$ (B) for the interaction of HNO_3 with α- and β-NAT films. We would like to briefly remind the reader that only TO experiments were possible for HNO_3 experiments. The following equations define the corresponding straight lines based on the present measurements. For α-NAT (Eqs. (17) and (18)) and β-NAT films (Eqs. (19) and (20)) we find the following results:

α-NAT: $$\log J_{ev}(HNO_3)[\text{molec}\cdot\text{cm}^{-2}\cdot\text{s}^{-1}] = (62.3 \pm 7.8) - \frac{(178.0 \pm 27.4)\times10^3}{2.303\ \text{RT}} \quad (17)$$

$$\log P_{ev}(HNO_3)[\text{Torr}] = (29.3 \pm 12.0) - \frac{(128.6 \pm 42.4)\times10^3}{2.303\ \text{RT}} \quad (18)$$

β-NAT: $$\log J_{ev}(HNO_3)[\text{molec}\cdot\text{cm}^{-2}\cdot\text{s}^{-1}] = (40.6 \pm 2.4) - \frac{(102.0 \pm 8.6)\times10^3}{2.303\ \text{RT}} \quad (19)$$

$$\log P_{ev}(HNO_3)[\text{Torr}] = (19.8 \pm 3.3) - \frac{(96.5 \pm 12.0)\times10^3}{2.303\ \text{RT}} \quad (20)$$

We calculate an activation energy for HNO_3 evaporation on α-NAT and β-NAT of $E_{ev}(HNO_3)$ = (178.0 ± 27.4) kJ mol^{-1} and $E_{ev}(HNO_3)$ = (102.0 ± 8.6) kJ mol^{-1}, respectively. These values are higher compared to $E_{ev}(HCl)$ = (87.0 ± 17) kJ mol^{-1}, the activation energy for HCl evaporation on hexahydrate. This result is within expectation given the higher hydrogen bond energy of HNO_3 compared to HCl with H_2O.

Similar to the case of H_2O, no activation energy for accommodation of HNO_3 on β-NAT is required since the evaporation activation energy $E_{ev}(HNO_3)$ = (102.0 ± 8.6) kJ mol^{-1} and the enthalpy of evaporation $\Delta H^0_{ev}(HNO_3)$ = (96.5 ± 12.0) kJ mol^{-1} are equal within experimental uncertainties. In contrast, a substantial activation energy of H_2O mass accommodation of 49.4 kJ/mol is calculated from $E_{acc}(H_2O) = E_{ev}(H_2O) - \Delta H^0_{ev,TO}(H_2O)$ = 178.0 – 128.6 = 49.9 kJ/mol which may have to do with the fact that α-NAT is metastable owing to its unstable H_2O crystal structure.

The thermodynamic parameters obtained above, namely $\Delta H^0_{ev}(H_2O)$ and $\Delta H^0_{ev}(HNO_3)$ for both α- and β-NAT may now be used to estimate the relative stability of α- vs. β-NAT as follows. The evaporation/condensation equilibrium for both forms of NAT may be

Atmos. Chem. Phys. Discuss., doi:10.5194/acp-2016-247, 2016
Manuscript under review for journal Atmos. Chem. Phys.
Published: 5 April 2016

Atmospheric Chemistry and Physics Discussions

represented in equation (21) where $\Sigma\Delta H_{ev}^{0} = 3\,\Delta H_{ev}^{0}(H_2O) + \Delta H_{ev}^{0}(HNO_3)$ in agreement with the relevant stoichiometry:

$$HNO_3 \bullet 3H_2O(s) \leftrightarrows 3H_2O(g) + HNO_3(g) \qquad (\Sigma\Delta H_{ev}^{0}) \qquad (21)$$

For α- and β-NAT we obtain $\Sigma\Delta H_{ev}^{0,\alpha}$ and $\Sigma\Delta H_{ev}^{0,\beta}$ equal to 318.8 and 324.8 kJ/mol, respectively, when we use the average of the TO and PV experiment for H_2O and the TO value listed above for HNO_3 evaporation. Specifically, we have used (63.4 ± 9.6) and (128.6 ± 42.2) for H_2O- and (76.1 ± 14.4) and (96.5 ± 12.0) for HNO_3-evaporation for α- and β-NAT, respectively, as displayed above. Finally, we arrive at the difference $\Sigma\Delta H_{ev}^{0,\alpha}$ - $\Sigma\Delta H_{ev}^{0,\beta}$ = -6.0 ± 20.0 kJ/mol which shows that β-NAT is marginally more stable than α-NAT. This is true despite the fact that the standard heat of evaporation for HNO_3 in α-NAT ($\Delta H_{ev}^{0}(HNO_3)$) is significantly larger than for β-NAT by 32.1 kJ/mol which may be expressed by the fact that the calculated "affinity" of HNO_3 towards ice in the α-NAT is larger than for β-NAT as claimed by Weiss et al. (2016). However, this fact only addresses the behavior of HNO_3 without taking into consideration the partial stability of the H_2O network in the total crystal structure. In view of the large uncertainty, mainly brought about by the TO experiment, we regard this result as an estimate to the true standard enthalpy difference between α- and β-NAT.

The results of HCl kinetic measurements displayed in Figure 6 and Figure 7 show that $R_{ev}(HCl)$ is always higher than $R_{ev}(HNO_3)$, with the latter being equal regardless of the presence of absorbed HCl molecules in the condensed phase. Hynes et al. (2002) also observed that HCl uptake on HNO_3 dosed ice was always nearly reversible in their experiments, in contrast to HCl uptake on clean ice. Although the same HNO_3 dosed ice surface has been dosed repeatedly at different HCl concentrations by Hynes et al. (2002), the degree of reversibility was found to be unaffected by previous experiments. In contrast, we never observed such reversibility. In our experiments, HCl always remained on the surface, evaporating at a rate only slightly faster than HNO_3 both for α-NAT and β-NAT and similarly to $R_{ev}(HCl)$ of crystalline hexahydrate (Iannarelli and Rossi, 2014). However, a possible influence of the temperature cannot be excluded at this time, as the experiments performed by Hynes et al. (2002) have been performed at distinctly higher temperatures, namely in the range 210-235 K, compared to the experiments discussed here.

Atmos. Chem. Phys. Discuss., doi:10.5194/acp-2016-247, 2016
Manuscript under review for journal Atmos. Chem. Phys.
Published: 5 April 2016

Atmospheric Chemistry and Physics Discussions

Similar behavior has been observed by Kuhs et al. (2012) with respect to the presence of cubic ice or "ice I_c" in common hexagonal ice I_h. I_h is expected to be the prevalent ice phase at temperatures relevant to atmospheric processing on thermodynamic grounds. Apparent formation of I_c has been observed over a wide temperature range and evidence pointed towards the fact that the resulting phase is not pure cubic ice but instead composed of disordered cubic and hexagonal stacking sequences. Kuhs et al. (2012) studied the extent and relevance of the stacking disorder using both neutron as well as X-ray diffraction as indicators of the "cubicity" of vapor deposited ice at temperatures from 175 to 240 K and could simply not find proof for the formation of cubic ice I_c under atmospheric conditions.

Kuhs et al. (2012) discovered that even at temperatures as high as 210 K, the fraction of cubic sequences in vapor deposited ice is still approximately 40%. The rate of decrease in cubicity depends on the temperature, being very slow at temperatures lower than 180 K and increasingly rapid at temperatures higher than 185 K. Furthermore, even at high temperatures the complete transformation into pure ice I_h was never observed, with a few percent of cubic stacking sequences still remaining in the ice, even after several hours at 210 K and disappeared only upon heating to 240 K. In addition, the combination of neutron and X-ray diffraction experiments of Kuhs et al. (2012) cannot distinguish the difference between the bulk and the interface whereas our measurement techniques, in particular PV experiments, are very sensitive to the nature and properties of the sample interface.

In light of these results we speculate that the presence of two hydrates of HNO_3, namely α-NAT and β-NAT, may depend on the cubicity or stack-disorder of the ice upon which the NAT grows. HNO_3 adsorbed on cubic ice I_c tends to form α-NAT crystalline structures which upon heating converts to β-NAT while the ice loses part of its cubicity. The temperature at which the conversion from α-NAT to β-NAT is accelerated, T = 185 K, is the same temperature Kuhs et al. (2012) report as the temperature at which the rate of decrease in cubicity increases. Our hypothesis is that the formation of α-NAT or β-NAT may highly depend on the environment in which the NAT phase grows and on the presence of high or low fractions of "I_c".

Figure 12 displays both the Arrhenius plots of J_{ev}(HCl) (A) and the van 't Hoff plots of P_{eq}(HCl) (B) for the interaction of HCl with α-NAT and β-NAT films. As for the case of HNO_3, only TO experiments were performed with HCl as a probe gas. Full red circles and black triangles represent the interaction of HCl with α- and β-NAT films, respectively.

Atmos. Chem. Phys. Discuss., doi:10.5194/acp-2016-247, 2016
Manuscript under review for journal Atmos. Chem. Phys.
Published: 5 April 2016

Atmospheric Chemistry and Physics Discussions

The following equations define the corresponding straight lines resulting from the present measurements. For α-NAT (Eqs. (22) and (23)) and β-NAT films (Eqs. (24) and (25)) we find the following results:

α-NAT: $$\log J_{ev}(HCl)[molec \cdot cm^{-2} \cdot s^{-1}] = (34.8 \pm 5.3) - \frac{(78.3 \pm 19.2)\times 10^3}{2.303\ RT} \quad (22)$$

$$\log P_{ev}(HCl)[Torr] = (15.7 \pm 3.2) - \frac{(78.4 \pm 11.4)\times 10^3}{2.303\ RT} \quad (23)$$

β-NAT: $$\log J_{ev}(HCl)[molec \cdot cm^{-2} \cdot s^{-1}] = (28.6 \pm 1.3) - \frac{(56.7 \pm 4.6)\times 10^3}{2.303\ RT} \quad (24)$$

$$\log P_{ev}(HCl)[Torr] = (13.3 \pm 1.6) - \frac{(69.6 \pm 5.8)\times 10^3}{2.303\ RT} \quad (25)$$

Despite the scatter of the data displayed in Figure 12 it may be pointed out that the enthalpy of HCl evaporation is identical for α- and β-NAT within the stated experimental uncertainty: We compare $\Delta H^0_{ev}(HCl)$ of 78.4 ± 11.4 and 69.6 ± 5.8 kJ/mol for α- and β-NAT (equations (23) and (25)). On the other hand we have equality, perhaps fortuitously, between $E_{ev}(HCl)$ and $\Delta H^0_{ev}(HCl)$ for α-NAT following equations (22) and (23) which leads to the expected conclusion that HCl accommodation on α-NAT is not an activated process which essentially has zero activation energy similar to the situation for HNO_3 interacting with β-NAT. On the other hand, this type of argument would lead to a negative activation energy for HCl accommodation on β-NAT because the enthalpy of evaporation of HCl from β-NAT is smaller than $E_{ev}(HCl)$ from β-NAT. However, the kinetic data of $J_{ev}(HCl)$ for β-NAT may be affected by saturation of HCl uptake because experiments have been performed using the PV admission. This situation may be similar to the kinetic results of $J_{ev}(H_2O)$ for β-NAT displayed in Figure 10 that shows a significantly smaller value for $E_{ev}(H_2O)$ in PV vs. TO experiments (52.1 vs. 75.5 kJ/mol, see also Table 3) whereas the saturation effect seems not to affect the kinetic data for α-NAT. The anomalously large experimental uncertainty for HNO_3 TO experiments on α-NAT displayed in Table 3 certainly has to do with the restricted temperature interval over which we were able to monitor α-NAT before it converted to β-NAT. This may be seen in the synoptic overview of the van't Hoff plots for HNO_3 interacting with NAT displayed in Figure S4 of Supplement D. This restricted T range is also visible in Figure 11A for $J_{ev}(HNO_3)$ from α-NAT.

Atmos. Chem. Phys. Discuss., doi:10.5194/acp-2016-247, 2016
Manuscript under review for journal Atmos. Chem. Phys.
Published: 5 April 2016

Atmospheric Chemistry and Physics Discussions

5 Conclusions and Atmospheric Implications

In this study we have confirmed that exposure of ice films to HNO_3 vapor pressures at temperatures akin to the ones found in the stratosphere leads to formation of NAT hydrates.

Of the two known forms of NAT, namely α-NAT and β-NAT, the latter is the thermodynamically stable one whereas metastable α-NAT is likely to be of lesser importance in the heterogeneous processes at UT/LS atmospherically relevant conditions.

$R_{ev}(H_2O)$ on α-NAT and β-NAT films are different compared to the case of HCl/ice where the evaporation of H_2O is not influenced by the presence of adsorbed HCl on the ice and takes place at a rate characteristic of pure ice. This has important implications on the lifetime of atmospheric ice particles. Ice particles with adsorbed HNO_3 forming NAT have longer lifetimes compared to ice particles with adsorbed HCl, being amorphous or crystalline $HCl{\bullet}6H_2O$. In light of our results we raise the question if HCl-containing ice particles are of significant atmospheric relevance as substrates for heterogeneous reactions due to their reduced lifetimes and concurrent reduced opportunities to enable heterogeneous atmospheric reactions.

$J_{ev}(H_2O)$ on α-NAT presents a discontinuity at 181 K akin to that observed in pure ice by Delval and Rossi (2004) and Pratte et al. (2006). The resulting Arrhenius representation at high temperatures larger than 181 ± 2 K:

$$\log J_{ev}(H_2O)[\text{molec}\cdot\text{cm}^{-2}\cdot\text{s}^{-1}] = (35.9 \pm 2.8) - \frac{(75.3 \pm 9.9)\times 10^3}{2.303\ \text{RT}}$$

$J_{ev}(H_2O)$ on β-NAT shows two values depending on the measurement techniques as a result of the propensity of the PV experiment to saturate the gas-condensate interface. TO experiments are less precise but more accurate owing to the fact that they are less prone to saturation compared to PV experiments. Therefore, we report results of TO experiments as preferred values, whereas we rule out kinetic PV results owing to possible saturation problems and note in passing that β-NAT is apparently prone to saturation than α-NAT. The Arrhenius representation for the preferred TO results is:

TO Experiments: $\log J_{ev}(H_2O)[\text{molec}\cdot\text{cm}^{-2}\cdot\text{s}^{-1}] = (36.0 \pm 1.3) - \frac{(77.0 \pm 4.9)\times 10^3}{2.303\ \text{RT}}$

HCl kinetic measurements on α-NAT and β-NAT indicate that HCl does not displace a significant number of HNO_3 molecules from the ice surface upon deposition, but rather that

Atmos. Chem. Phys. Discuss., doi:10.5194/acp-2016-247, 2016
Manuscript under review for journal Atmos. Chem. Phys.
Published: 5 April 2016

Atmospheric Chemistry and Physics Discussions

HCl and HNO_3 do not strongly interact with each other in the condensed phase and that HCl evaporates faster. This observation is also supported by the slower rates of evaporation and the correspondingly higher values of the HNO_3 evaporation activation energy on α-NAT and β-NAT, $E_{ev}(HNO_3)$ = (178.0 ± 27.4) kJ mol^{-1} and $E_{ev}(HNO_3)$ = (102.0 ± 8.6) kJ mol^{-1} (see Table 3), respectively, compared to the activation energy for HCl evaporation on HCl•$6H_2O$, $E_{ev}(HCl)$ = (87.0 ± 17) kJ mol^{-1}. This also is consistent with a larger calculated interaction energy of HNO_3 with H_2O ("affinity") in α-NAT compared to β-NAT (Weiss et al., 2016) despite the fact that ΔH_f^0(α-NAT) is higher by 6 ± 20 kJ/mol compared to β-NAT.

The reliable and reproducible measurement of the vapor pressure of H_2O (P_{H2O}) in the UT/LS still represents a thorny problem on airborne (aircraft and balloon) platforms owing to small absolute values as well as to possible rapid variations as a function of altitude. Fahey and coworkers have found an elegant way to solve this problem using a suitably adapted chilled mirror hygrometer (CMH) where a cryogenic ice deposit on a temperature controlled mirror is monitored during atmospheric sampling using a backreflected IR LED element that controls a mirror heater in a feed-back loop (Thornberry et al., 2011). When $\mathbf{P_{H_2O}}$ increases the mirror reflectivity decreases owing to a concomitant, but presumed increase in scattering because of the formation of a polycrystalline ice deposit on the mirror. In this case the mirror heating power is increased in a feedback loop in order to restore the original reflectivity at the former operating conditions.

For concentrations of 1-10 ppm H_2O and 0.1-4 ppb HNO_3 typically encountered in this region of the atmosphere (UT/LS) we expect a weak perturbation of the cryogenic ice deposit through co-deposition of HNO_3 on the mirror. In fact, Thornberry et al. (2011) measure a HNO_3 deposit from their laboratory experiment corresponding to roughly a molecular monolayer on the 0.37 cm^2 mirror (geometric) surface at typically 4 ppb P_{HNO3} and a total deposition time of 3 h. This is a negligible quantity of HNO_3 compared to the 2000 or so ice molecular bilayers per μm of ice deposited. Fahey and coworkers have recently introduced an advanced version of a hygrometer that monitors gas phase H_2O using a high resolution diode laser near 2694 nm at a specific H_2O absorption line (Thornberry et al., 2015). This methodology replaces the unspecific monitoring of the broad-band reflectivity by an identifiable spectroscopic molecular IR transition of gas phase H_2O and thus removes the doubt about the identity of the absorber compared to the prior use of the (broad band) IR

Atmos. Chem. Phys. Discuss., doi:10.5194/acp-2016-247, 2016
Manuscript under review for journal Atmos. Chem. Phys.
Published: 5 April 2016

Atmospheric Chemistry and Physics Discussions

878 LED. It is our understanding that this advanced CMH is in the process of actually being tested
879 in the field.

880 However, when the CMH was used in a laboratory flow reactor experiment at a higher
881 concentration of H_2O and HNO_3 (both at typically 80 ppb) the mirror reflectivity increased
882 and led to an approximately 3 K lower mirror temperature at 194 K after approximately 4
883 hours into the experiment compared to a reference CMH not exposed to HNO_3. At first, the
884 authors identified the first HNO_3/H_2O condensate as an α-NAT coating on a H_2O thin film
885 after approximately 1.8 hours into the co-deposition experiment of admitting six ppm H_2O
886 and 80 ppb HNO_3 into the flow reactor. At 2.3 hours after start the HNO_3 flow was halted
887 while maintaining a H_2O flow of 80 ppm which led to the appearance of a "second
888 condensate" after approximately 4 hours of elapsed time. The authors attributed this "second
889 condensate" to an unknown HNO_3/H_2O phase that led to a 63% supersaturation with respect
890 to pure ice corresponding to the above-mentioned 3 K depression of the mirror temperature.

891 It is perhaps useful to remind the reader at this point that the CMH detector of $\mathbf{P_{H_2O}}$
892 compensates the change in reflectivity detected as a signal on a photodiode with a change in
893 mirror temperature, but the true molecular identity of the condensate goes unnoticed. Based
894 on the present results we claim that the selective evaporation of the heavier components
895 HNO_3 compared to H_2O evaporation in the binary, and HCl in the ternary condensed phase
896 system is not possible, at least at atmospherically relevant HNO_3 and HCl concentrations
897 because $J_{ev}(HNO_3)$ and $J_{ev}(HCl)$ are always smaller than $J_{ev}(H_2O)$ for the investigated nitric
898 acid hydrates in the range 170-205 K. This means that the "second condensate" must still
899 contain some HNO_3 throughout the duration of the experiment. As far as positive proof for
900 the existence of an as yet unidentified HNO_3/H_2O hydrate ("second condensate") is concerned
901 that results from the CMH-equipped flow experiment discussed above, we would like to
902 withhold judgement until possible consequences of the optical properties of the HNO_3/H_2O
903 condensate on the reported H_2O supersaturation have been considered, including its temporal
904 changes at the chosen experimental conditions.

905 Using the real part of the index of refraction n at approximately 200 K of 1.333, 1.513 and
906 1.460 for pure H_2O ice, α- and β-NAT, respectively [Berland et al., 1994; Toon et al., 1994],
907 we calculate a specular reflectivity R of 2.0, 4.2 and 3.5% for pure H_2O ice, α- and β-NAT
908 following the Fresnel expression ($R = (n_0-n_1)^2/(n_0+n_1)^2$) with n_0 referred to pure H_2O ice) for
909 normal incidence. This shows that a potentially significant change of the optical properties of

a HNO_3-containing ice film relative to pure ice may be expected at these high doses of HNO_3, which will critically depend on many geometric and molecular parameters including the structure and concentration gradients of the film itself.

The implementation of a detailed (geometrical) optical model of the cryogenic film interacting with the IR-emission is clearly beyond the scope of the present work, but it seems judicious to take these optical changes into account in the future for the quantitative interpretation of the experimental results of Gao et al. (2016). In addition, it will be necessary to gauge the importance of film volume absorption as the emitted IR radiation will pass twice across the film thickness on its way to the detector. We have recently measured the optical cross sections of the nitric acid hydrates dealt with in the present work in the range 4000-750 cm^{-1} (Iannarelli and Rossi, 2015) which completes the set of optical constants of the nitric acid hydrates in the IR spectral region (Toon et al., 1994). In the end the decision on the existence of an unknown/unidentified HNO_3/H_2O phase present in the UT/LS that significantly exceeds the saturation vapor pressure of pure ice will probably hinge on experiments performed using the advanced version of the hygrometer that is based on the absorption of high resolution radiation near 2.7 μm by gas phase water vapor mentioned above. This gas-phase measurement system seems free of perturbations by other atmospheric gases and therefore is likely to be suitable in order to resolve the question at hand (Thornberry et al., 2015).

Acknowledgements

The authors would like to acknowledge the generous support of this work over the years by the Swiss National Science Foundation (SNSF) in the framework of projects 200020_125204 and 200020_144431/1. We also sincerely thank Mr. Alwin Frei of PSI for graciously granting the permission to perform the experiments in his laboratory. In addition, our warm thanks go to Mr. René Richter and Günther Wehrle for hardware and IT support so sorely needed.

References

Berland, B.S., Haynes, D.R., Foster, K.L., Tolbert, M.A., George S.M. and Toon, O.B.: Refractive Indices of Amorphous and Crystalline HNO_3/H_2O Films Representative of Polar Stratospheric Clouds, J. Phys. Chem., 98, 4358-4364, 1994.

Biermann, U.M., Crowley J.N., Huthwelker T., Moortgat G.K., Crutzen P.J. and Peter T.: FTIR studies on lifetime prolongation of stratospheric ice particles due to NAT coating, Geophys. Res. Lett., 25(21), 3939–3942, 1998.

Chaix, L., van den Bergh, H. and Rossi, M.J.: Real-Time kinetic measurements of the condensation and evaporation of D_2O molecules on ice at 140 K < T < 220 K, J. Phys. Chem. A, 102(50), 10300–10309, 1998.

Crowley, J.N., Ammann, M., Cox, R.A., Hynes, R.G., Jenkin, M.E., Mellouki, A., Rossi, M.J., Troe, J. and Wallington, T.J.: Evaluated kinetic and photochemical data for atmospheric chemistry: Volume V – heterogeneous reactions on solid substrates, Atmos. Chem. Phys., 10, 9059-9223, 2010.

Chiesa, S. and Rossi, M.J.: The metastable $HCl•6H_2O$ phase – IR spectroscopy, phase transitions and kinetic/thermodynamic properties in the range 170-205 K, Atmos. Chem. Phys., 13(23), 11905–11923, 2013; doi:10.5194/acp-13-11905-2013.

Delval, C., Flückiger, B. and Rossi, M.J.: The rate of water vapor evaporation from ice substrates in the presence of HCl and HBr: implications for the lifetime of atmospheric ice particles, Atmos. Chem. Phys., 3, 1131–1145, 2003.

Delval, C. and Rossi, M.J.: The kinetics of condensation and evaporation of H_2O from pure ice in the range 173-223 K: A quartz crystal microbalance study, Phys. Chem. Chem. Phys., 6: 4665–4676, 2004.

Delval, C. and Rossi, M.J.: Influence of monolayer amounts of HNO_3 on the evaporation rate of H_2O over ice in the range 179 to 208 K: A quartz crystal microbalance study, J. Phys. Chem. A, 109(32), 7151–7165, 2005.

Escribano, R.M., Fernandez-Torre, D., Herrero, V.J., Martin-Llorente, B., Maté, B., Ortega, I. K. and Grothe, H.: The low-frequency Raman and IR spectra of nitric acid hydrates, Vibr. Spectry., 43, 254–259, 2007.

967 Fahey, D.W., Gao, R.S., Carslaw, K.S., Kettleborough, J., Popp, P.J., Northway, M.J.,
968 Holecek, J.C., Ciciora, S.C., McLaughlin, R.J., Thompson, T.L., Winkler, R.H.,
969 Baumgardner, D.G., Gandrud, B., Wennberg, P.O., Dhaniyala, S., McKinney, K., Peter, T.,
970 Salawitch, R.J., Bui, T.P., Elkins, J.W., Webster, C.R., Atlas, E.L., Jost, H., Wilson, J.C.,
971 Herman, R.L., Kleinböhl, A. and von König, M.: The Detection of Large HNO_3-Containing
972 Particles in the Winter Arctic Stratosphere, Science, 291, 1026-1031, 2001.

973 Friedel, R. A., Shultz, J. L. and Sharkey, A. G.: Mass spectrum of nitric acid, Anal. Chem.,
974 31(6), 1128–1128, 1959.

975 Gao, R.S., Popp, P.J., Fahey, D.W., Marcy, T.P., Herman, R.L., Weinstock, E.M.,
976 Baumgardner, D.G., Garrett, T.J., Rosenlof, K.H., Thompson, T.L., Bui, P.T., Ridley, B.A.,
977 Wofsy, S.C., Toon, O.B., Tolbert, M.A., Kärcher, B., Peter, Th., Hudson, P.K., Weinheimer,
978 A.J. and Heymsfield, A.J.: Evidence That Nitric Acid Increases Relative Humidity in Low-
979 Temperature Cirrus Clouds, Science 303, 516-520, 2004.

980 Gao, R.S., Gierczak, T., Thornberry, T.D., Rollins, A.W., Burkholder, J.B., Telg, H., Voigt,
981 C., Peter, T. and Fahey, D.W.: Persistent Water-Nitric Acid Condensate with Saturation
982 Water Vapor Pressure Greater than That of Hexagonal Ice, J. Phys. Chem. A, 120, 1431-
983 1440, 2016.

984 Hamill, P., Turco, R.P. and Toon, O.B.: On the growth of nitric and sulfuric acid aerosol
985 particles under stratospheric conditions, J. Atmos. Chem., 7(3), 287–315, 1988.

986 Hanson, D.R. and Mauersberger, K.: Laboratory studies of the nitric acid trihydrate:
987 Implications for the south polar stratosphere, Geophys. Res. Lett., 15(8), 855–858, 1988.

988 Hanson, D.R.: The uptake of HNO_3 onto Ice, NAT and frozen sulfuric acid, Geophys. Res.
989 Lett., 19(20), 2063–2066, 1992.

990 Herrero, V.J., Ortega, I.K., Maté, B., Martin-Llorente, B., Escribano, R. and H. Grothe:
991 Comment on “Theoretical investigation of the coexistence of α- and β-nitric acid trihydrates
992 (NAT) molecular conformation” [Chem. Phys., 324 (2006) 210], Chem. Phys., 331, 186–188,
993 2006.

994 Höpfner, M., Luo, B.P., Massoli, P., Cairo, F., Spang, R., Snels, M., Di Donfrancesco, G.,
995 Stiller, G., von Clarmann, T., Fischer, H. and Biermann, U.M.: Spectroscopic evidence for
996 NAT, STS, and ice in the MIPAS infrared limb emission measurements of polar stratospheric
997 clouds, Atmos. Chem. Phys., 6, 1201-1219, 2006.

998 Hynes, R.G., Fernandez, M.A. and Cox, R.A.: Uptake of HNO_3 on water-ice and co-
999 adsorption of HNO_3 and HCl in the temperature range 210–235 K, J. Geophys. Res. Atmos.,
1000 107(D24), AAC 19–1 to AAC 19–11, 2002.

1001 Iannarelli, R. and Rossi, M.J.: H_2O and HCl trace gas kinetics on crystalline HCl hydrates and
1002 amorphous HCl/H_2O in the range 170 to 205 K: the HCl/H_2O phase diagram revisited, Atmos.
1003 Chem. Phys., 14(10), 5183-5204, 2014.

1004 Iannarelli, R. and Rossi, M.J.: The mid-IR Absorption Cross Sections of α- and β-NAT
1005 (HNO_3•$3H_2O$) in the range 170 to 185 K and of metastable NAD (HNO_3•$2H_2O$) in the range
1006 172 to 182 K, J. Geophys. Res. Atmos., 120, 11707-11727, 2015.

1007 Ji, K. and Petit, J.-C., Calorimetric Identification of a new Nitric Acid hydrate able to play a
1008 Role in the Heterogeneous Chemistry of the Stratosphere, Compt. Rend. Acad. Sci. Ser II,
1009 316(12), 1743-1748, 1993.

1010 Koehler, B.G., Middlebrook, A.M. and Tolbert, M.A.: Characterization of model polar
1011 stratospheric cloud films using Fourier transform infrared spectroscopy and temperature
1012 programmed desorption, J. Geophys. Res., 97(D8), 8065–8074, 1992.

1013 Kuhs, W. F., Sippel, C., Falenty, A. and Hansen, T.C.: Extent and relevance of stacking
1014 disorder in "ice I_c", PNAS, 109(52), 21259– 21264, 2012.

1015 Marti, J. and Mauersberger, K.: A survey and new measurements of ice vapor pressure at
1016 temperatures between 170 and 250 K, Geophys. Res. Lett., 20, 363–366, 1993.

1017 Martin-Llorente, B., Fernandez-Torre, D., Herrero, V.J., Ortega, I.K., Escribano, R. and Maté,
1018 B.: Vibrational spectra of crystalline hydrates of atmospheric relevance: Bands of hydrated
1019 protons, Chem. Phys. Lett., 427, 300–304, 2006.

1020 Mauersberger, K. and Krankowsky, D.: Vapor pressure above ice at temperatures below 170
1021 K, Geophys. Res. Lett., 30(3), 1121, 2003.

1022 McElroy, M.B., Salawitch, R.J. and Wofsy, S.C.: Antarctic O_3: Chemical mechanisms for the
1023 spring decrease. Geophys. Res. Lett., 13(12), 1296–1299, 1986.

1024 McNeill, V.F., Loerting, T., Geiger, F.M., Trout, B.L. and Molina, M.J.: Hydrogen chloride-
1025 induced surface disordering on ice, PNAS, 103(25), 9422–9427, 2006.

1026 McNeill, V.F., Geiger, F.M., Loerting, T., Trout, B.L., Molina, L.T. and Molina, M.J.:
1027 Interaction of hydrogen chloride with ice surfaces: the effects of grain size, surface roughness,
1028 and surface disorder. J. Phys. Chem. A, 111(28), 6274–6284, 2007.

1029 Middlebrook, A.M., Koehler, B.G., McNeill, L.S. and Tolbert, M.A.: Formation of model
1030 polar stratospheric cloud films, Geophys. Res. Lett., 19(24), 2417–2420, 1992.

1031 Molina, L.T., Molina M.J., Stachnik, R.A. and Tom, R.D.: An upper limit to the rate of the
1032 HCl + $ClONO_2$ reaction, J. Phys. Chem., 89, 3779-3781, 1985.

1033 Molina, M.J., Tso, T.L., Molina, L.T. and Wang, F.C.Y.: Antarctic stratospheric chemistry of
1034 chlorine nitrate, hydrogen chloride and ice: release of active chlorine, Science, 238, 1253-
1035 1257, 1987.

1036 Molina, M.J.: The Probable Role of Stratospheric 'Ice' Clouds: Heterogeneous Chemistry of
1037 the Ozone Hole, in "The Chemistry of the Atmosphere: Its Impact on Global Change",
1038 Blackwell Scientific Publications, London, ch. 3, pp 27- 38, 1994.

1039 Moussa, S.G., Kuo, M.H. and McNeill, V.F.: Nitric acid-induced surface disordering on ice,
1040 Phys. Chem. Chem. Phys., 15, 10989–10995, 2013.

1041 Ortega, I.K., Escribano, R., Fernandez, D., Herrero, V.J., Maté, B., Medialdea, A. and
1042 Moreno, M.A.: The structure and vibrational frequencies of crystalline nitric acid, Chem.
1043 Phys. Lett., 378, 218–223, 2003.

1044 Ortega, I.K., Maté, B., Moreno, M.A., Herrero, V.J. and Escribano, R.: Infrared spectra of
1045 nitric acid trihydrate (β-NAT): A comparison of available optical constants and implication
1046 for the detection of polar stratospheric clouds (PSC's), Geophys. Res. Lett., 33 L19816, 2006.

1047 Peter, T.: Microphysics and heterogeneous chemistry of Polar Stratospheric Clouds, Ann.
1048 Rev. Phys. Chem., 48, 785-822, 1997.

1049 Pratte P., van den Bergh H. and Rossi, M.J.: The kinetics of H_2O vapor condensation and
1050 evaporation on different types of ice in the range 130-210 K, J. Phys. Chem A, 110(9), 3042–
1051 3058, 2006.

1052 Reinhardt, H., Fida, M. and Zellner, R.: DRIFTS-studies of the interactions of HNO_3 with ice
1053 and HCl (HNO_3)-hydrate surfaces at temperatures around 165 K, J. Mol. Struct., 661–662,
1054 567–577, 2003.

1055 Ritzhaupt, G. and Devlin, J.P.: Infrared spectra of nitric and hydrochloric acid hydrate thin
1056 films, J. Phys. Chem., 95, 90-95, 1991.

1057 Schreiner, J., Voigt, C., Kohlmann, A., Arnold F., Mauersberger, K. and Larsen, Niels:
1058 Chemical Analysis of Polar Stratospheric Cloud Particles, Science, 283, 968-970, 1999.

1059 Schreiner, J., Voigt, C., Weisser, C., Kohlmann, A., Mauersberger, K., Deshler, T., Kröger,
1060 C., Rosen, J., Kjome, N., Larsen, N., Adriani, A., Cairo, F., Di Donfrancesco, G., Ovarlez, J.,
1061 Ovarlez, H. and Dörnbrack, A.: Chemical, microphysical, and optical properties of polar
1062 stratospheric clouds, J. Geophys. Res., 108(D5), 8313, 2003.

1063 Solomon, S., Garcia, R.R., Rowland, F.S. and Wuebbles, D.J.: On the depletion of Antarctic
1064 ozone, Nature, 321, 755-758, 1986.

1065 Solomon, S.: Progress towards a quantitative understanding of Antarctic ozone depletion,
1066 Nature, 347, 347-354, 1990.

1067 Thornberry, T.D., Gierczak, T., Gao, R.S., Vömel, H., Watts, L.A., Burkholder, J.B. and
1068 Fahey, D.W.: Laboratory evaluation of the effect of nitric acid uptake on frost point
1069 hygrometer performance, Atmos. Meas. Tech., 4, 289-296, 2011.

1070 Thornberry, T.D., Rollins, A.W., Gao, R.S., Watts, L.A., Ciciora, S.J., McLaughlin, R.J. and
1071 Fahey, D.W.: A two-channel, tunable diode laser-based hygrometer for measurement of water
1072 vapor and cirrus cloud ice water content in the upper troposphere and lower stratosphere,
1073 Atmos. Meas. Tech., 8, 211-224, 2015

1074 Tolbert, M.A. and Middlebrook, A.M.: Fourier transform infrared studies of model polar
1075 stratospheric cloud surfaces: Growth and evaporation of ice and nitric acid/ice, J. Geophys.
1076 Res., 95(D13), 22423–22431, 1990.

1077 Tolbert, M.A., Koehler, B.G. and Middlebrook, A.M.: Spectroscopic studies of model polar
1078 stratospheric cloud films, Spectrochim. Acta Part A: Mol. Spectrosc., 48(9), 1303–1313,
1079 1992.

1080 Toon, O.B., Tolbert, M.A., Koehler, B.G., Middlebrook, A.M. and Jordan, J.: Infrared optical
1081 constants of H_2O ice, amorphous nitric acid solutions, and nitric acid hydrates, Geophys. Res.,
1082 99(D12), 25631-25654 (1994).

1083 Tso, T.-L. and Leu, M.-T.: Quantitative analysis of the infrared absorptivities of nitric acid
1084 ices existing in polar stratospheric clouds, Anal. Sci., 12, 615–622, 1996.

1085 Voigt, C., Schreiner, J., Kohlmann, A., Zink, P., Mauersberger, K., Larsen, N., Deshler, T.,
1086 Kröger, C., Rosen, J., Adriani, A., Cairo, F., Di Donfrancesco, G., Viterbini, M., Ovarlez, J.,
1087 Ovarlez, H., David, C. and Dörnbrack, A.: Nitric Acid Trihydrate (NAT) in Polar
1088 Stratospheric Clouds, Science, 290, 1756-1758, 2000.

1089 Voigt, C., Schlager, H., Luo, B.P., Dörnbrack, A., Roiger, A., Stock, P., Curtius, J., Vössing,
1090 H., Borrmann, S., Davies, S., Konopka, P., Schiller, C., Shur, G. and Peter, T.: Nitric Acid
1091 Trihydrate (NAT) formation at low NAT supersaturation in Polar Stratospheric Clouds
1092 (PSC's), Atmos. Chem. Phys., 5, 1371-1380, 2005.

1093 Weiss, F., Kubel, F., Gálvez, O., Hoelzel, M., Parker, S.F., Iannarelli, R., Rossi, M.J. and
1094 Grothe, H.: Metastable Nitric Acid Trihydrate in Ice Clouds, Angewandte Chemie I.E., 55,
1095 3276-3280, 2016; doi: 10.1002/anie.201510841, 2016.

1096 Wooldridge, P.J., Zhang, R. and Molina, M.J.: Phase equilibria of H_2SO_4, HNO_3, and HCl
1097 hydrates and the composition of polar stratospheric clouds, J. Geophys. Res. Atmos.,
1098 100(D1), 1389–1396, 1995.

1099 Zondlo, M.A., Barone, S.B. and Tolbert, M.A.: Condensed-phase products in heterogeneous
1100 reactions: N_2O_5, $ClONO_2$, and HNO_3 reacting on ice films at 185 K, J. Phys. Chem. A, 102,
1101 5735–5748, 1998.

1102 Zondlo, M.A., Hudson, P.K., Prenni, A.J. and Tolbert, M.A.: Chemistry and microphysics of
1103 polar stratospheric clouds and cirrus clouds, Ann. Rev. Phys. Chem., 51, 473-499, 2000.
1104

Atmos. Chem. Phys. Discuss., doi:10.5194/acp-2016-247, 2016
Manuscript under review for journal Atmos. Chem. Phys.
Published: 5 April 2016

Atmospheric Chemistry and Physics Discussions

Table 1: Characteristic parameters of the present flow reactor.

Reactor volume (upper chamber)	$\mathbf{V_R}$ = 2036 cm^3		
MS (lower) chamber	$\mathbf{V_{MS}}$ = 1750 cm^3		
Reactor internal surface	$\mathbf{S_W}$ = 1885 cm^2		
H_2O calibrated volume – inlet line	$\mathbf{V_{water}}$ = 62 cm^3		
HNO_3 calibrated volume – inlet line	$\mathbf{V_{acid}}$ = 20 cm^3		
Si support area (one side)	$\mathbf{A_{Si}}$ = 0.99 cm^2		
Surface to Volume ratio	$\mathbf{2\ A_{Si}/V_R}$ = 0.9725×10^{-4} cm^{-1}		
Reactor wall temperature	$\mathbf{T_w}$ = 315 K		
Conversion of evaporation rate and flux	$\mathbf{R_{ev} \cdot V_R = 2 \cdot A_{Si} \cdot J_{ev}}$		
	HNO_3	**H_2O**	**HCl**
Base Peak Signal MS [m/z]	46	18	36
MS Calibration Factor $\mathbf{C^X}$ [$molec^{-1}$ s A]	4.53×10^{-25}	6.65×10^{-25}	1.30×10^{-25}
Escape rate constant $k_{esc}^{S} = C^{S}\sqrt{\frac{T}{M}}$ (small orifice) [s^{-1}]	0.0913	0.1710	0.1213
$k_{esc}^{M} = C^{M}\sqrt{\frac{T}{M}}$ (both orifices) [s^{-1}]	0.4331	0.8102	0.5729
Gas-surface collision frequency at 315 K, one side [s^{-1}] [(a)] $\omega = \frac{\bar{c}}{4V}\cdot A_{Si} = \sqrt{\frac{8\,R\,T}{\pi\,M}}\cdot\frac{A_{Si}}{4V}$	3.95	7.39	5.22

[(a)] M in kg; A_{Si} in m^2; V in m^3; R = 8.314 J K^{-1} mol^{-1}. "One side" corresponds to front or rear side of Si-window. In order to calculate the accommodation coefficient α using equation (3) we have used 2ω as the total collision frequency for both sides of the Si-window.

Atmos. Chem. Phys. Discuss., doi:10.5194/acp-2016-247, 2016
Manuscript under review for journal Atmos. Chem. Phys.
Published: 5 April 2016

Atmospheric Chemistry and Physics Discussions

Table 2: Fit parameters of the Langmuir adsorption isotherms for H_2O, HNO_3 and HCl interaction with the internal stainless steel (SS304) surfaces of the reactor.

Adsorbed Gas (Additional Gas) [(a)]	**K_L** [$\times10^{-14}$] [(b)]	**N_{TOT}** [$\times10^{17}$] [(c)]	**N_{MAX}** [$\times10^{14}$] [(d)]	**α_w** [$\times10^{-6}$] [(e)]
H_2O	3.18 ± 0.38	7.03 ± 0.42	3.73 ± 0.22	6.19 ± 0.08
H_2O (HCl, F_{in} = 8×10^{14})	4.67 ± 0.39	8.38 ± 0.29	4.45 ± 0.15	–
HNO_3	1.10 ± 0.16	93 ± 11	49 ± 6	2.92 ± 0.10
HNO_3 (H_2O, F_{in} = $2\text{-}3\times10^{15}$)	1.61 ± 0.40	76 ± 15	40 ± 8	–
HNO_3 (average values)	1.28 ± 0.17	84 ± 8	45 ± 4	–
HCl	437 ± 21	5.06 ±0.06	2.68 ± 0.03	16.9 ± 0.3
HCl (H_2O, F_{in} = 6×10^{15})	63.1 ± 4.9	4.85 ± 0.07	2.57 ± 0.04	–
HCl (H_2O, F_{in} = 3×10^{15})	64.6 ± 6.3	3.79 ± 0.09	2.01 ± 0.04	–

[(a)] F_{in} is the flow rate of the additional gas in molec s^{-1}.

[(b)] K_L is the Langmuir adsorption equilibrium constant in cm^3 $molec^{-1}$.

[(c)] N_{TOT} is the total number of adsorbed molecules onto the internal surfaces, reported is the saturation value for total internal surface (1885 cm^2) of SFR.

[(d)] N_{MAX} is the adsorption site density in molec cm^{-2}.

[(e)] α_w is the reactor wall accommodation coefficient.

Atmos. Chem. Phys. Discuss., doi:10.5194/acp-2016-247, 2016
Manuscript under review for journal Atmos. Chem. Phys.
Published: 5 April 2016

Atmospheric Chemistry and Physics Discussions

Table 3: Synopsis of thermodynamic (P_{eq}) and kinetic (J_{ev}) parameters of the Arrhenius and van 't Hoff representation of data from Figure 2, Figure 4, Figure 6 and Figure 7.

			J_{ev} [a]		P_{eq} [b]	
			E_{ev}	A	ΔH^0_{ev}	$\Delta S/R$
Sample	**Gas**	**Exp.**				
α-NAT	H_2O	TO	75.3 ± 9.9[c] 3.5 ± 4.2[c]	35.9 ± 2.8	70.3 ± 14.1	15.2 ± 4.0
		PV	75.3 ± 9.9[c] 3.5 ± 4.2[c]	15.1 ± 1.2	56.5 ± 5.1	11.8 ± 1.5
	HNO_3	TO	178.0 ± 27.4	62.3 ± 7.8	128.6 ± 42.4	29.3 ± 12.0
	HCl	PV	78.3 ± 19.2	34.8 ± 5.3	78.4 ± 11.4	15.7 ± 3.2
β-NAT	H_2O	TO	77.0 ± 4.9	36.0 ± 1.3	76.7 ± 17.7	16.7 ± 4.9
		PV	52.1 ± 2.4	28.7 ± 0.7	75.5 ± 11.1	16.7 ± 3.0
	HNO_3	TO	102.0 ± 8.6	40.6 ± 2.4	96.5 ± 12.0	19.8 ± 3.3
	HCl	PV	56.7 ± 4.6	28.6 ± 1.3	69.6 ± 5.8	13.3 ± 1.6

[a] for gas X, R = 8.314 J K^{-1} mol^{-1}: $\log J_{ev}(X)[\text{molec} \cdot \text{cm}^{-2} \cdot \text{s}^{-1}] = A - \frac{E_{ev} \times 10^3}{2.303\ RT}$

[b] for gas X, R = 8.314 J K^{-1} mol^{-1}: $\log P_{ev}(X)[\text{Torr}] = \frac{\Delta S}{R} - \frac{\Delta H^0_{ev} \times 10^3}{2.303\ RT}$

[c] Fit consists of two straight lines intersecting at 181 ± 2 K with two values for E_{ev}.

Atmos. Chem. Phys. Discuss., doi:10.5194/acp-2016-247, 2016
Manuscript under review for journal Atmos. Chem. Phys.
Published: 5 April 2016

Atmospheric Chemistry and Physics Discussions

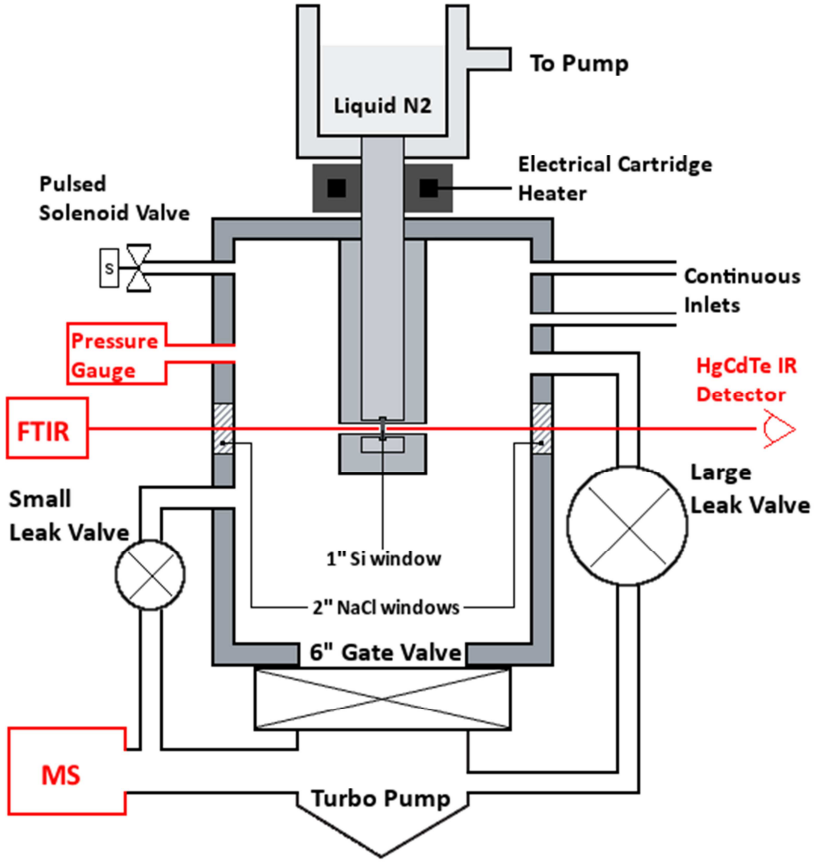

1126

1127 Figure 1: Schematic drawing of the reactor used in this work. The diagnostic tools are
1128 highlighted in red and important parameters are listed in Table 1 and Table 2. The ice film is
1129 deposited on both sides of the 1" diameter Si window (black vertical symbol hanging from
1130 cryostat inside reaction vessel).

1131

Atmos. Chem. Phys. Discuss., doi:10.5194/acp-2016-247, 2016
Manuscript under review for journal Atmos. Chem. Phys.
Published: 5 April 2016

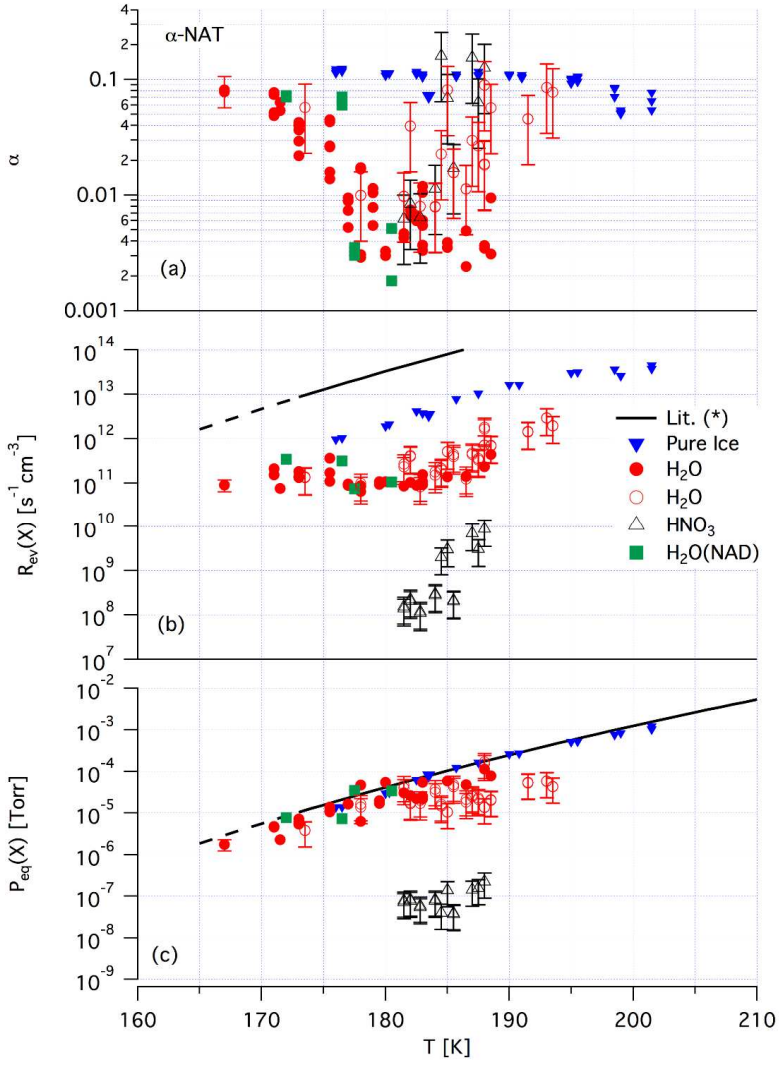

Figure 2: Synopsis of kinetic results for α-NAT and NAD using H_2O as a probe gas in PV experiments and H_2O and HNO_3 in two-orifice (TO) experiments. Full symbols represent PV experiments and empty symbols represent TO experiments. Further explanations of the used symbols may be found in the text. The calculated relative error for PV experiments is 30% whereas for TO experiments we estimate a relative error of 60%. Examples of the amplitude of the errors are reported for selected points. The black line shows results from Marti and Mauersberger (1993) with $R_{ev}(H_2O)$ of pure ice calculated for the system in use using $\alpha = 1$.

Atmos. Chem. Phys. Discuss., doi:10.5194/acp-2016-247, 2016
Manuscript under review for journal Atmos. Chem. Phys.
Published: 5 April 2016

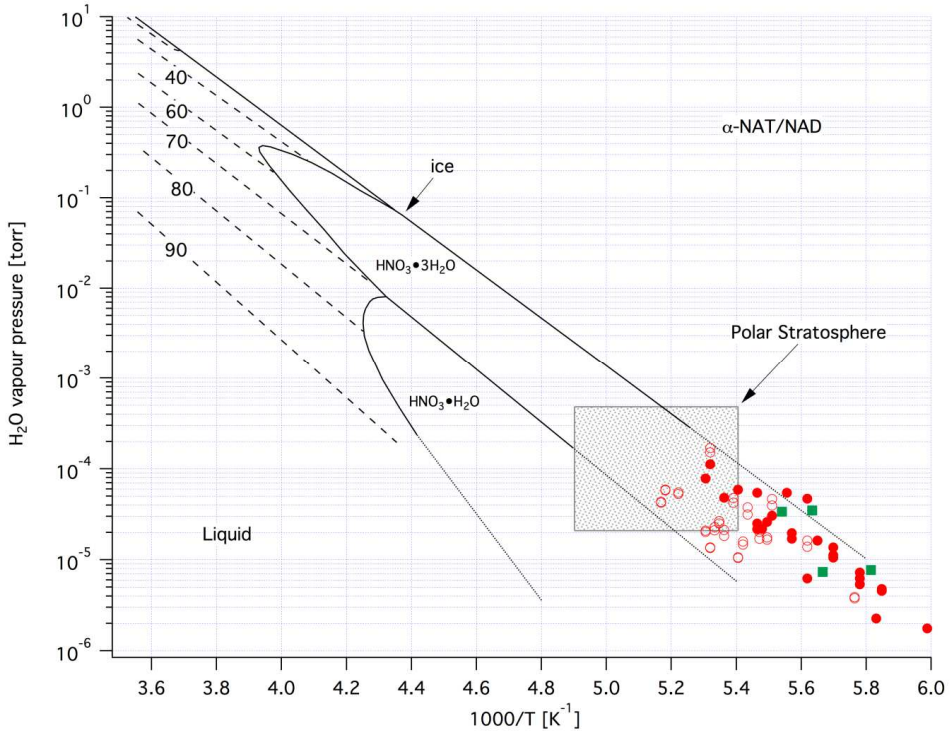

Figure 3: Binary phase diagram of the HNO_3/H_2O system reconstructed from McElroy et al. (1986); Hamill et al. (1988); Molina (1994). The full symbols represent calculated values of $P_{eq}(H_2O)$ for α-NAT and NAD using the kinetic data of PV experiments. Empty circles represent calculated values of $P_{eq}(H_2O)$ for α-NAT using the kinetic data of two-orifice experiments. The solid lines represent the coexistence conditions for two phases and the dashed lines represent vapor pressures of liquids with composition given as % (w/w) of HNO_3. The shaded gray represents polar stratospheric conditions.

Atmos. Chem. Phys. Discuss., doi:10.5194/acp-2016-247, 2016
Manuscript under review for journal Atmos. Chem. Phys.
Published: 5 April 2016

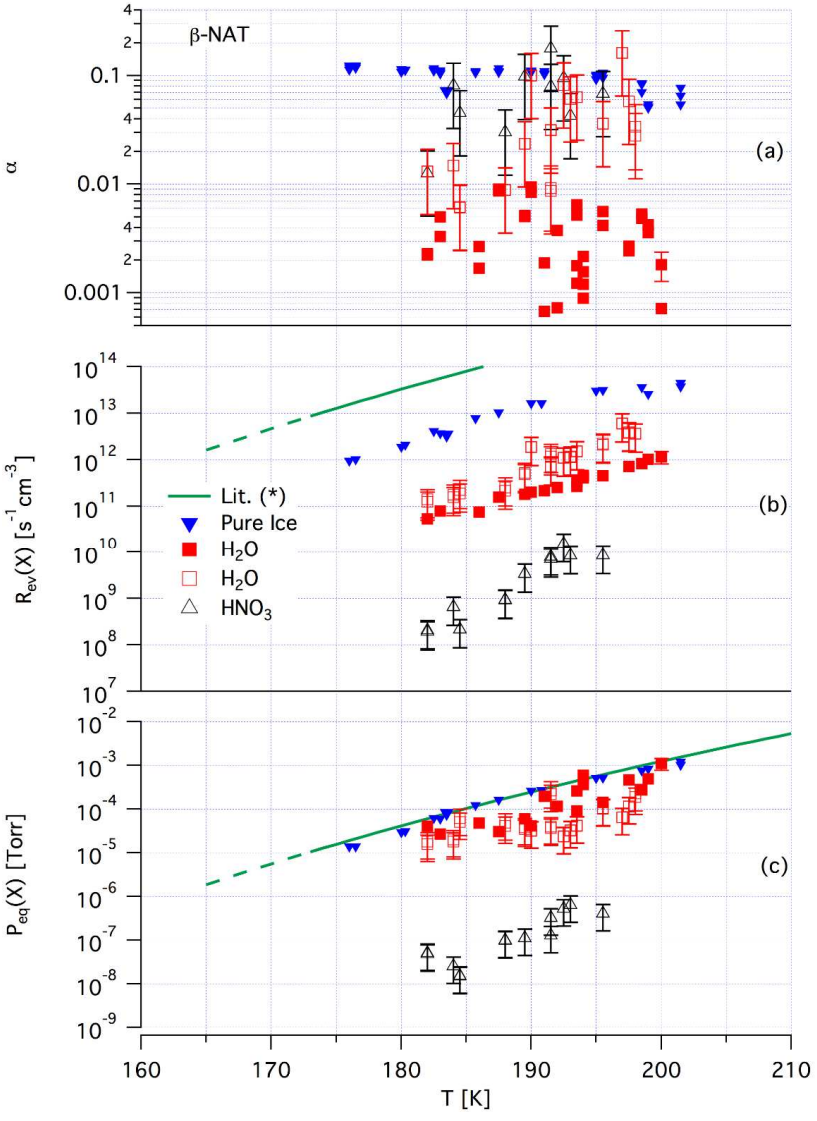

Figure 4: Synopsis of kinetic results for β-NAT using H_2O as a probe gas in PV experiments and H_2O and HNO_3 in two-orifice experiments. Full symbols represent PV experiments and empty symbols represent TO experiments. Further explanation of the used symbols may be found in the text. The calculated relative error for PV experiments is 30% whereas for TO experiments we estimate a relative error of 60%. Examples of the amplitude of the errors are reported for selected points. The green line shows results from Marti and Mauersberger (1993).

Atmos. Chem. Phys. Discuss., doi:10.5194/acp-2016-247, 2016
Manuscript under review for journal Atmos. Chem. Phys.
Published: 5 April 2016

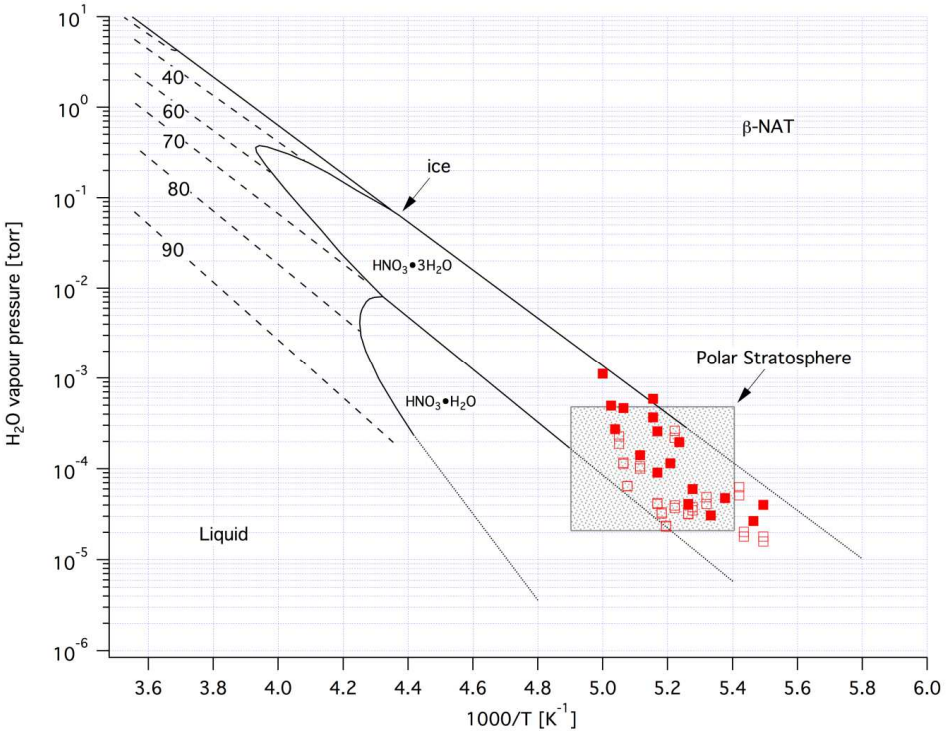

Figure 5: Binary phase diagram of the HNO_3/H_2O system reconstructed from McElroy et al. (1986); Hamill et al. (1988); Molina (1994). The full symbols represent calculated values of $P_{eq}(H_2O)$ for β-NAT using the kinetic data of PV experiments. Empty circles represent calculated values of $P_{eq}(H_2O)$ using the kinetic data of two-orifice experiments. The solid lines represent the coexistence conditions for two phases and the dashed lines represent vapor pressures of liquids with composition given as % (w/w) of HNO_3. The shaded gray represents polar stratospheric conditions.

Atmos. Chem. Phys. Discuss., doi:10.5194/acp-2016-247, 2016
Manuscript under review for journal Atmos. Chem. Phys.
Published: 5 April 2016

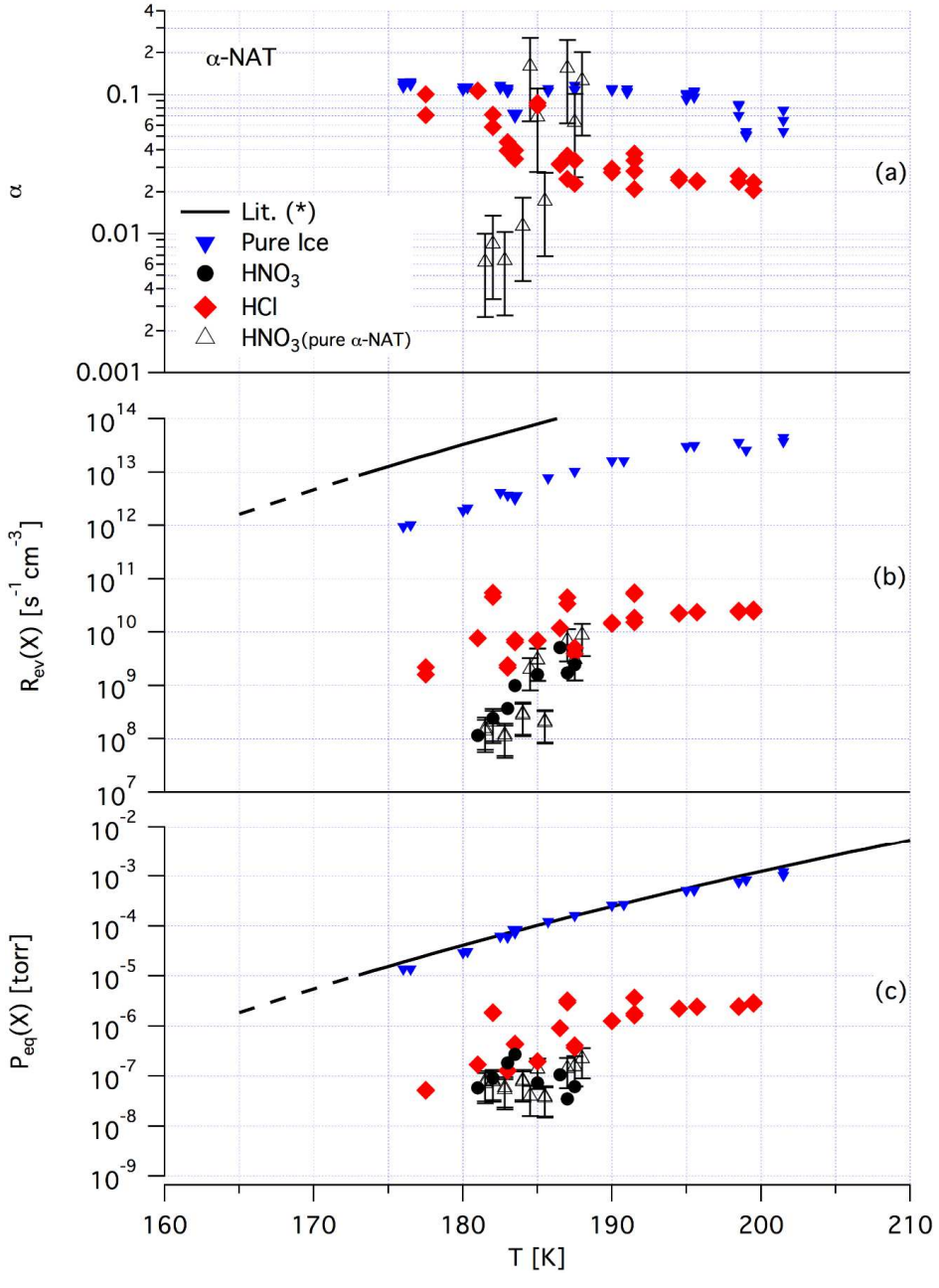

Figure 6: Synopsis of kinetic results for α-NAT using HCl as a probe gas in PV experiments. The used symbols are explained in the text. The calculated relative error for PV experiments is 30%. The black line shows results from Marti and Mauersberger (1993).

Atmos. Chem. Phys. Discuss., doi:10.5194/acp-2016-247, 2016
Manuscript under review for journal Atmos. Chem. Phys.
Published: 5 April 2016

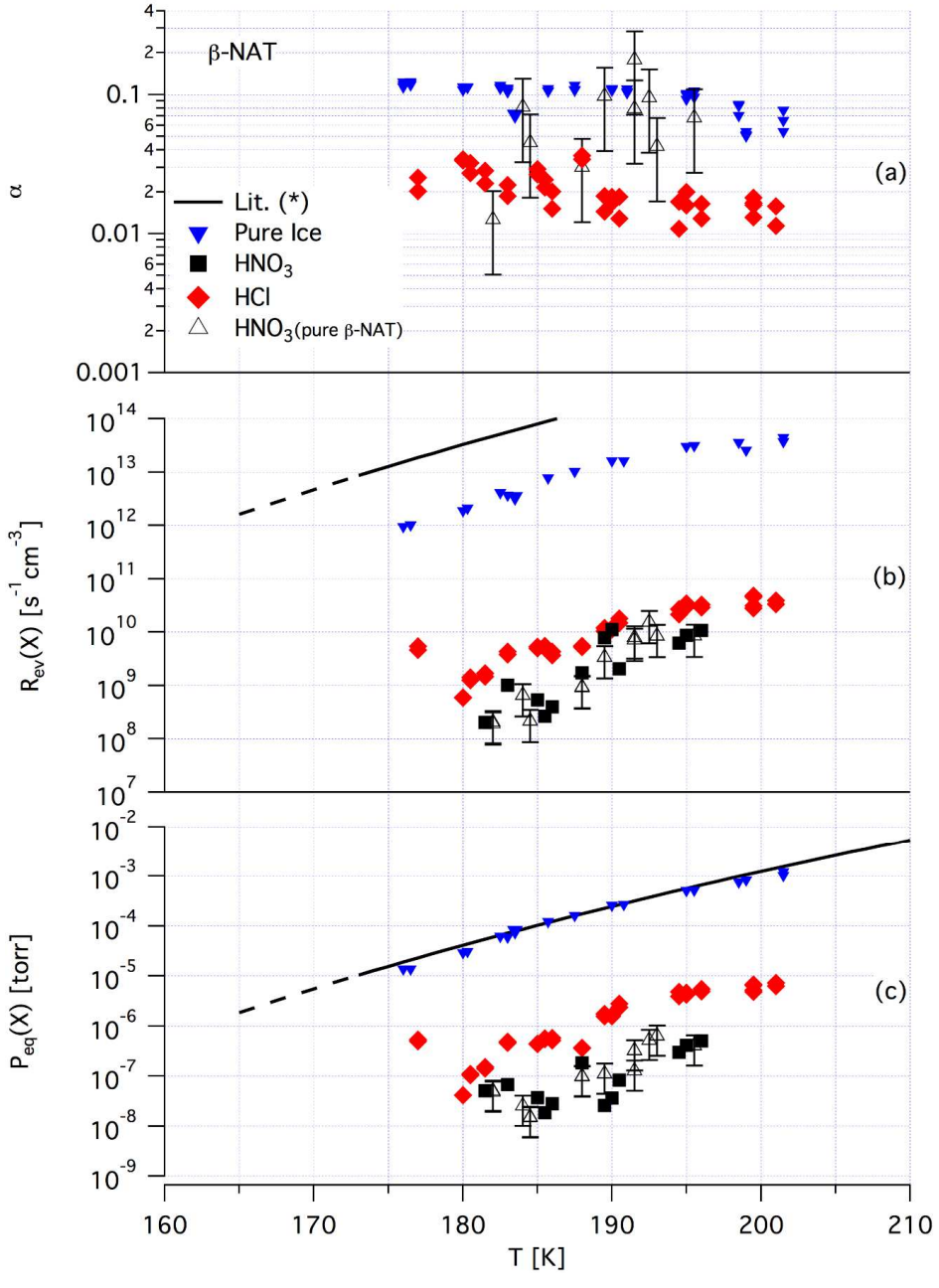

Figure 7: Synopsis of kinetic results for β-NAT using HCl as a probe gas in PV experiments. The used symbols are explained in the text. The calculated relative error for PV experiments is 30%. The black line shows results from Marti and Mauersberger (1993).

Atmos. Chem. Phys. Discuss., doi:10.5194/acp-2016-247, 2016
Manuscript under review for journal Atmos. Chem. Phys.
Published: 5 April 2016

Atmospheric Chemistry and Physics Discussions

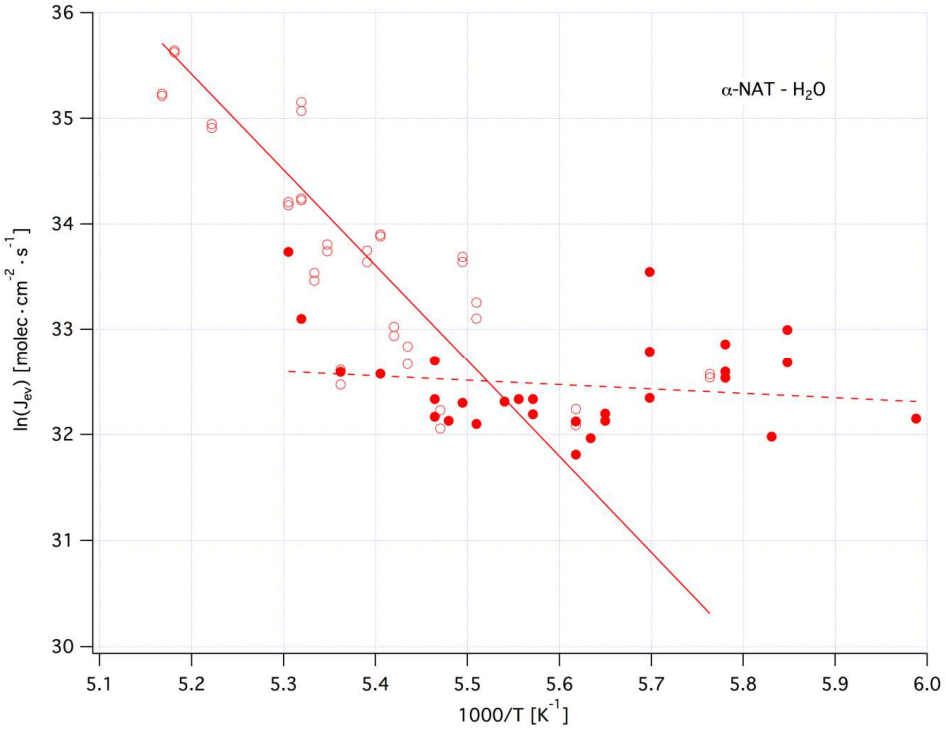

1172

1173 Figure 8: Arrhenius plot of $J_{ev}(H_2O)$ for α-NAT. Full and empty red circles represent results
1174 of PV and TO experiments, respectively. Data are taken from Figure 2b and the equations for
1175 the linear fits may be found in the text.

Atmos. Chem. Phys. Discuss., doi:10.5194/acp-2016-247, 2016
Manuscript under review for journal Atmos. Chem. Phys.
Published: 5 April 2016

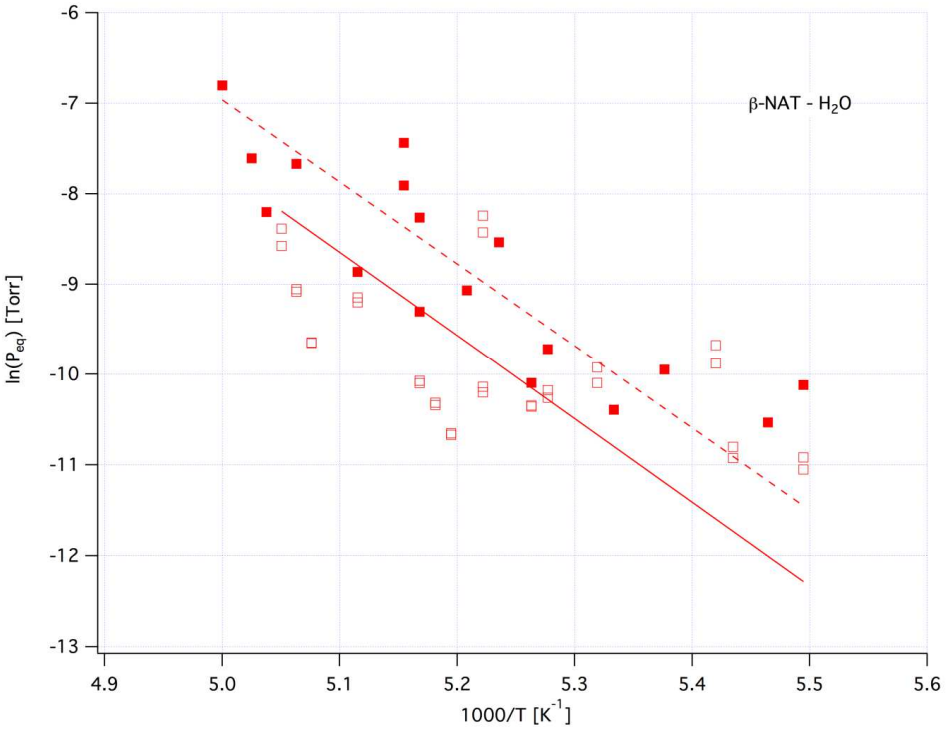

Figure 9: van 't Hoff plot of $P_{ev}(H_2O)$ for β-NAT data displayed in Figure 4c. Full and empty red squares represent results of PV and TO experiments, respectively. The equations for the linear fits may be found in the text.

Atmos. Chem. Phys. Discuss., doi:10.5194/acp-2016-247, 2016
Manuscript under review for journal Atmos. Chem. Phys.
Published: 5 April 2016

Atmospheric Chemistry and Physics Discussions

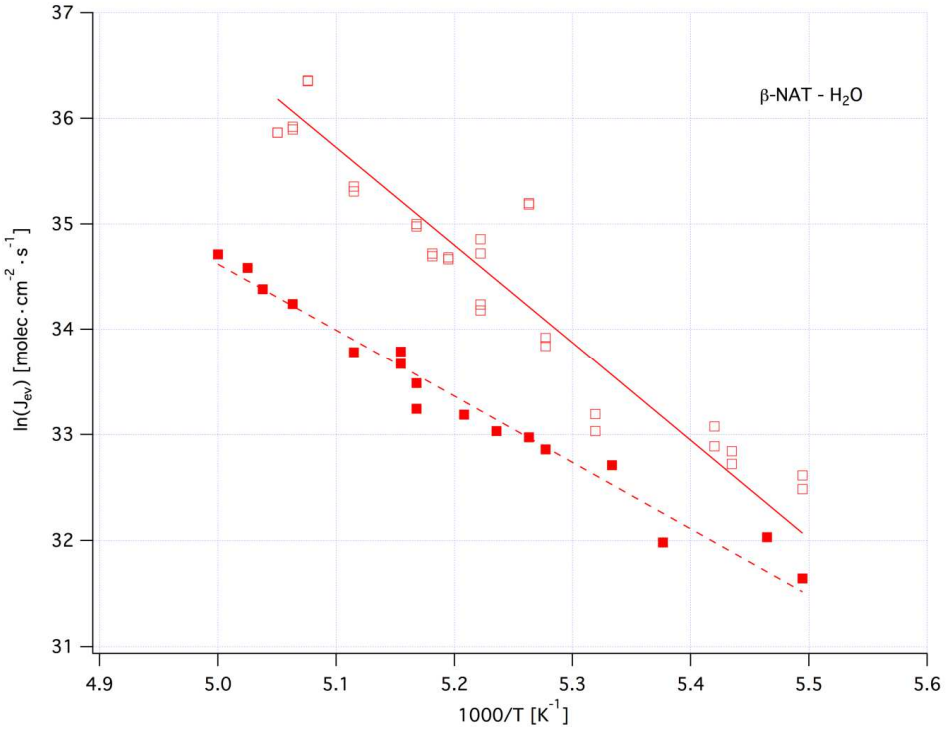

1180

1181 Figure 10: Arrhenius plot of $J_{ev}(H_2O)$ for β-NAT data displayed in Figure 4b. Full and empty
1182 red squares represent results of PV and TO experiments, respectively. The equations for the
1183 linear fits may be found in the text.

Atmos. Chem. Phys. Discuss., doi:10.5194/acp-2016-247, 2016
Manuscript under review for journal Atmos. Chem. Phys.
Published: 5 April 2016

Atmospheric Chemistry and Physics Discussions

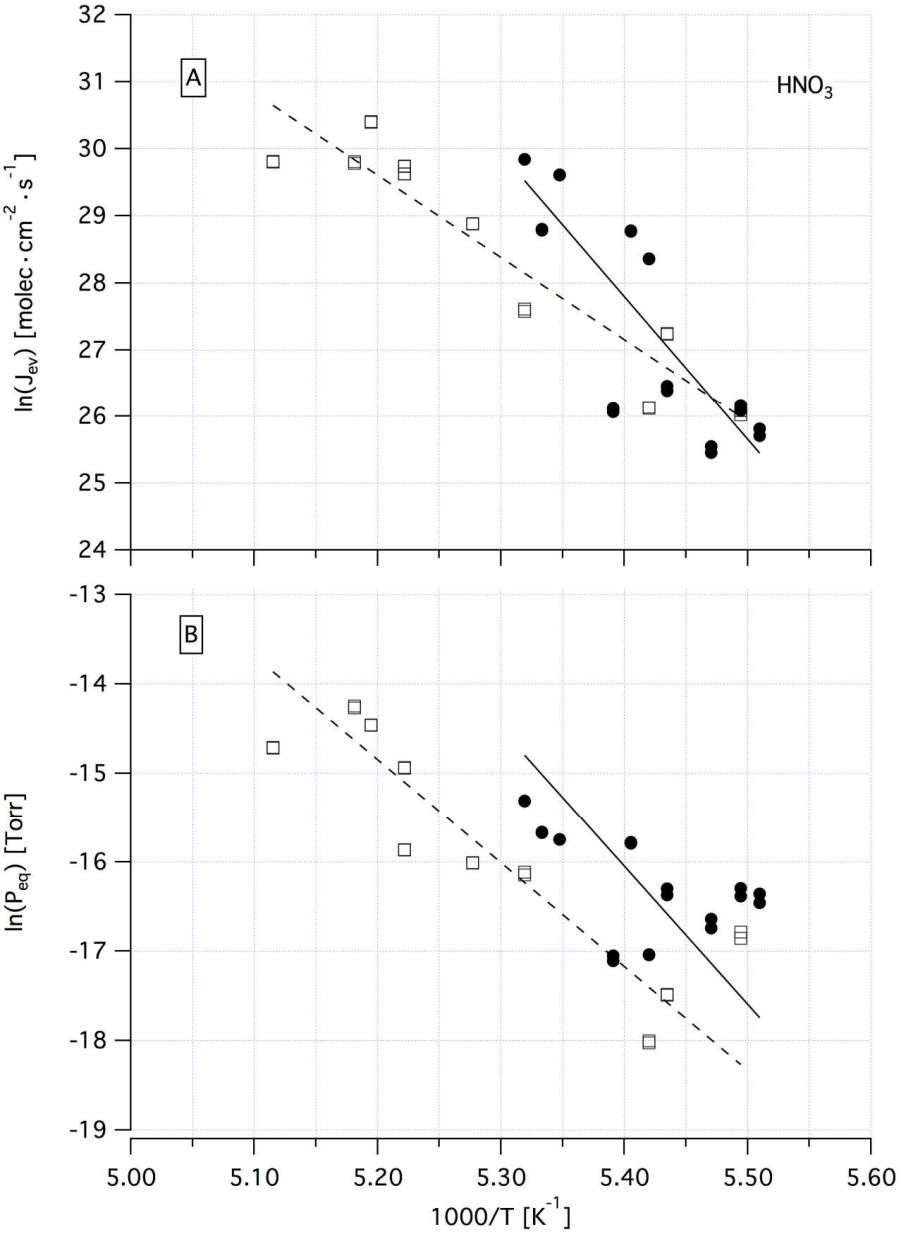

1184

1185 Figure 11: Arrhenius plot of $J_{ev}(HNO_3)$ (A) and van 't Hoff plot of $P_{eq}(HNO_3)$ (B) for α-NAT
1186 (Figure 2b and Figure 2c) and β-NAT (Figure 4b and Figure 4c) resulting from TO
1187 experiments. Full black circles and empty black squares represent the interaction of HNO_3
1188 with α- and β-NAT films, respectively. The equations for the fitting lines may be found in the
1189 text.

Atmos. Chem. Phys. Discuss., doi:10.5194/acp-2016-247, 2016
Manuscript under review for journal Atmos. Chem. Phys.
Published: 5 April 2016

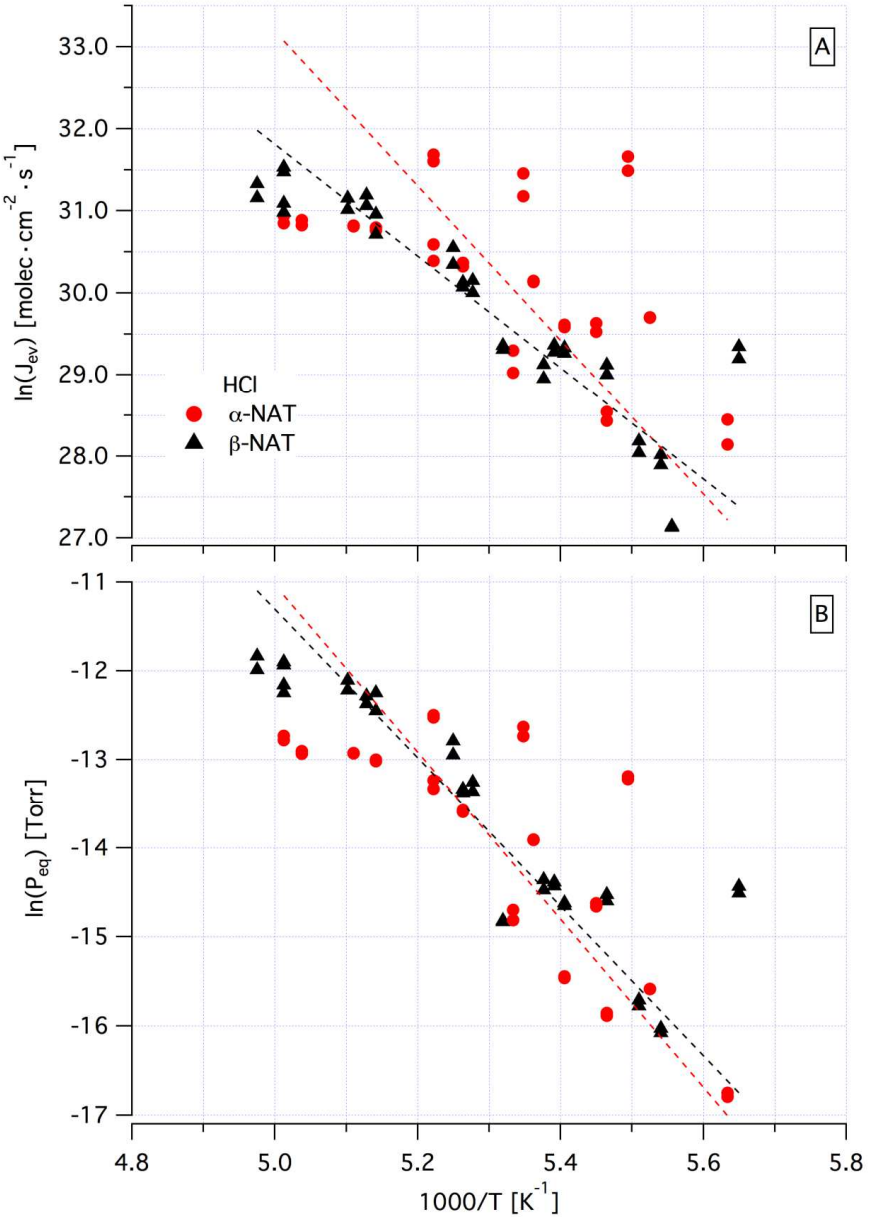

Figure 12: Arrhenius plot of J_{ev}(HCl) (A) and van 't Hoff plot of P_{eq}(HCl) (B) for α-NAT (Figure 6b and Figure 6c) and β-NAT (Figure 7b and Figure 7c) resulting from PV experiments. Full red circles and black triangles represent the interaction of HCl with α- and β-NAT films, respectively. The equations for the fitting lines may be found in the text.